Medical Image Analysis 77 (2022) 102356

Contents lists available at ScienceDirect

Medical Image Analysis

journal homepage: www.elsevier.com/locate/media

Moment-based representation of the diffusion inside the brain from reduced DMRI acquisitions: Generalized AMURA

Santiago Aja-Fernández[a,#,*], Tomasz Pieciak[a,b], Carmen Martín-Martín[a], Álvaro Planchuelo-Gómez[a], Rodrigo de Luis-García[a], Antonio Tristán-Vega[a]

[a] LPI, ETSI Telecomunicación, Universidad de Valladolid, Castilla y León, Spain
[b] AGH University of Science and Technology, Kraków, Poland

ARTICLE INFO

Article history:
Received 29 July 2021
Revised 13 December 2021
Accepted 6 January 2022
Available online 10 January 2022

Keywords:
Diffusion MRI
AMURA
Diffusion anisotropy
Fast acquisition
White matter

ABSTRACT

AMURA (Apparent Measures Using Reduced Acquisitions) was originally proposed as a method to infer micro-structural information from single-shell acquisitions in diffusion MRI. It reduces the number of samples needed and the computational complexity of the estimation of diffusion properties of tissues by assuming the diffusion anisotropy is roughly independent on the b-value. This simplification allows the computation of simplified expressions and makes it compatible with standard acquisition protocols commonly used even in clinical practice. The present work proposes an extension of AMURA that allows the calculation of general moments of the diffusion signals that can be applied to describe the diffusion process with higher accuracy. We provide simplified expressions to analytically compute a set of scalar indices as moments of arbitrary orders over either the whole 3-D space, particular directions, or particular planes. The existing metrics previously proposed for AMURA (RTOP, RTPP and RTAP) are now special cases of this generalization. An extensive set of experiments is performed on public data and a clinical clase acquired with a standard type acquisition. The new metrics provide additional information about the diffusion processes inside the brain.

1. Introduction

The name Diffusion Magnetic Resonance Imaging (DMRI) describes a set of diverse MRI imaging techniques with the ability of extracting *in vivo* relevant information regarding the random, anisotropic diffusion of water molecules that underlie the structured nature of different living tissues (Tournier et al., 2011; Assemlal et al., 2011; De Luca et al., 2021). It has attracted an extraordinary interest among the scientific community over the last two decades due to the relationships found between a number of neurological and neurosurgical pathologies and alterations in the white matter as revealed by an increasing number of DMRI studies (Rovaris and Filippi, 2007; Bester et al., 2015; Pasternak et al., 2015; Planchuelo-Gómez et al., 2020a; Planchuelo-Gomez et al., 2020).

In practice, in order to estimate the properties of the diffusion from the acquired data, different techniques can be adopted, being the diffusion tensor (Basser et al., 1994, DT) the most common in clinical studies. However, the diffusion mechanisms cannot be fully described by DT because of the oversimplified Gaussian fitting. More evolved techniques with more degrees-of-freedom have been proposed, such as Diffusion Kurtosis Imaging (Jensen et al., 2005, DKI) or methods based on High Angular Resolution Diffusion Imaging (Tuch et al., 2003; Özarslan et al., 2006; Canales-Rodríguez et al., 2010, HARDI). The trend over the last decade has been to acquire a large number of diffusion-weighted images distributed over several shells (i.e. with several gradient strengths) and with moderate-to-high b-values to estimate more advanced diffusion descriptors, such as the Ensemble Average diffusion Propagator (Descoteaux et al., 2011; Özarslan et al., 2013; Ning et al., 2015; Haije et al., 2020, EAP). This estimation relies on model-free, non parametric approaches that can accurately describe most of the relevant diffusion phenomena.

* Corresponding author.
E-mail addresses: sanaja@tel.uva.es (S. Aja-Fernández), pieciak@lpi.tel.uva.es (T. Pieciak), carmenmartinvi@gmail.com (C. Martín-Martín), a.planchuelo.gomez@gmail.com (Á. Planchuelo-Gómez), rluigar@gmail.com (R. de Luis-García), atriveg@lpi.tel.uva.es (A. Tristán-Vega).
ORCID: 0000-0002-5337-5071

https://doi.org/10.1016/j.media.2022.102356

Regardless of the method selected for estimating the diffusion properties, in order to be used in clinical studies, the information provided is usually translated into a set of scalar metrics such as: the Fractional Anisotropy (FA) or Mean Diffusivity (MD) (Basser and Pierpaoli, 1996; Westin et al., 2002) for the DT approach, the Kurtosis coefficient for DKI (Jensen et al., 2005; Lu et al., 2006) or the return-to-origin (RTOP), the return-to-plane (RTPP), return-to-axis probabilities (RTAP) and mean-squared-displacement (MSD) (Wu et al., 2008; Descoteaux et al., 2011; Özarslan et al., 2013; Hosseinbor et al., 2013; Ning et al., 2015), or the Propagator Anisotropy (PA) (Özarslan et al., 2013) for EAP imaging.

There are two main limitations with those techniques that rely on the estimation of the EAP: (1) the need of acquiring very large data sets with many **q**–space samples in different shells; and (2) the estimation of the EAP involves important computational burdens with very long processing times. These two issues have slowed down the generalization of this methodology among the clinical community, despite the relevance of its scalar measures in the description of the brain micro-structure, see for instance (Boscolo Galazzo et al., 2018; Brusini et al., 2016; Ma et al., 2020; Le et al., 2020). In order to overcome these problems, in (Aja-Fernández et al., 2020; 2021) authors proposed a new technique called "Apparent Measures Using Reduced Acquisitions" (AMURA) for the computation of EAP imaging-related markers, namely RTOP, RTPP, RTAP and PA without explicitly calculating the EAP. AMURA can mimic the sensitivity of EAP-based measures to microstructural changes when a reduced amount of data distributed in a few shells (even one) is available. In order to do so, AMURA assumes a prior model for the behavior of the radial **q**–space instead of trying to numerically describe it, yielding simplified expressions that can be computed easily even from single-shell acquisitions. It has proved its potential in some preliminary studies with clinical data (Parkinson and Mild Cognitive Impairment Aja-Fernández et al., 2020; Aja-Fernández et al., 2021) and recently in real clinical studies in migraine and headache (Planchuelo-Gómez et al., 2020b; 2021).

The present work proposes a generic formulation of AMURA that allows the calculation of generalized moments that can be better suited to describe certain anatomies, both healthy and pathological. The existing metrics (RTOP, RTPP and RTAP) can be seen as special cases of this generalization. To that end, the same constrained model for radial diffusion used by Aja-Fernández et al. (2020) is adopted here, i.e., the diffusion anisotropy is assumed to be independent of the actual b-value of the measured shells. We use this simplification to derive alternative simplified expressions for the moments of the acquired magnitude signal and the EAP from single-shell acquisitions.

Our hypothesis is that the new metrics based on moments representation provide extra information about the diffusion that can highlight additional interesting properties of certain brain structures compared to AMURA. In order to evaluate whether the calculation of general moments can be used as an alternative approach to standard AMURA in the analysis of specific brain regions, an extensive set of experiments was performed on data acquired with a typical acquisition protocol employed in a clinical context.

2. Background

2.1. The diffusion signal

The EAP, $P(\mathbf{R})$, is the three dimensional Probability Density Function (PDF) of the water molecules inside a voxel moving an effective distance $\mathbf{R}$ in an effective time τ. It is related to the normalized magnitude image provided by the MRI scanner, $E(\mathbf{q})$, by the Fourier transform (Callaghan et al., 1988):

$$P(\mathbf{R}) = \int_{\mathbb{R}^3} E(\mathbf{q}) \exp(-2\pi\, j\mathbf{q}^T\mathbf{R}) d\mathbf{q}. \tag{1}$$

The inference of exact information on the **R**–space would require the sampling of the whole **q**–space to use the Fourier relationship between both spaces.

In order to obtain an analytical solution from a reduced number of acquired images, a model for the diffusion behavior must be adopted. The most common techniques rely on the assumption of a Gaussian diffusion profile and a steady state regime of the diffusion process that yields to the well-known Diffusion Tensor (DT) approach. Alternatively, a more general expression for $E(\mathbf{q})$ can be used (Özarslan et al., 2006; Aja-Fernández et al., 2020):

$$E(\mathbf{q}) = \exp\left(-4\pi^2\tau q^2 D(\mathbf{q})\right) = \exp\left(-b \cdot D(\mathbf{q})\right), \tag{2}$$

where the positive function $D(\mathbf{q}) = D(q, \theta, \phi) > 0$ is the Apparent Diffusion Coefficient (ADC), $b = 4\pi^2\tau\|\mathbf{q}\|^2$ is the so-called b-value and $q = \|\mathbf{q}\|$, $\theta \in [0, 2\pi)$, and $\phi \in [0, \pi]$ are the angular coordinates in the spherical system. According to Basser (2002), in the mammalian brain this mono-exponential model is predominant for values of b up to 2000 s/mm^2 and it can be extended to higher values (up to 3000 s/mm^2) if appropriate multi-compartment models of diffusion are used.

2.2. Advanced diffusion measures from single shell acquisitions: AMURA

Despite the advantages of the EAP-based measures, the calculation of these scalars usually requires long execution and acquisition times, together with very large b-values and a large number of diffusion gradients, not always available in commercial scanners and generally discarded in the clinical routine. To solve these problems, AMURA has been developed in Aja-Fernández et al. (2020, 2021). This approach allows the estimation of simplified versions of EAP-related scalars without the explicit calculation of the EAP, using a lower number of samples, even with a single-shell acquisition scheme. AMURA considers that, if the amount of data is reduced, a restricted diffusion model consistent with single-shell acquisitions must be assumed: the ADC does not depend on the magnitude of **q** (i.e., it is roughly independent on the b-value) within the range of b-values probed, so that $D(\mathbf{q}) = D(\mathbf{u})$, where $\mathbf{u} \in \mathcal{S}$ is a unit direction in space where $||\mathbf{u}|| = 1$ and $\mathbf{q} = q\mathbf{u}$. This way Eq. (2) becomes:

$$E(\mathbf{q}) = E(q\mathbf{u}) = \exp\left(-4\pi^2\tau q^2\ D(\mathbf{u})\right). \tag{3}$$

This methodology allows shorter MRI acquisitions and very fast calculation of scalars. From Eq. (3), AMURA proposed a particular implementation of scalar measures. Since the mono-exponential model only holds within a limited range around the measured b-value, the measures derived this way must be seen as *apparent* values at a given b-value, related to the original ones but dependent on the selected shell. The main metrics defined in AMURA are:

1. **Return-to-origin probability (RTOP):** also known as probability of zero displacement, it is related to the probability density of water molecules that minimally diffuse within the diffusion time τ (Assaf et al., 2000; Wu et al., 2008; Hosseinbor et al., 2012). It is defined as the value of $P(\mathbf{R})$ at the origin, related to the volume of the signal $E(\mathbf{q})$:

$$\begin{aligned} \text{RTOP} &= \textstyle\int_{\mathbb{R}^3} E(\mathbf{q}) d\mathbf{q} \\ &= \frac{1}{(4\pi)^2\tau^{3/2}}\ C_{0,0}\left\{D(\mathbf{u})^{-3/2}\right\}. \end{aligned} \tag{4}$$

where $C_{0,0}\{H(\mathbf{u})\}$ is the zeroth-order coefficient of a spherical harmonics (SH) expansion of signal $H(\mathbf{u})$, defined as:

$$C_{0,0}\{H(\mathbf{u})\} = \frac{1}{\sqrt{4\pi}} \int_{\mathcal{S}} H(\mathbf{u}) d\mathbf{u}, \tag{5}$$

where $\mathcal{S}$ denotes the surface of a sphere of radius one.

2. **Return-to-plane probability (RTPP)**: defined as

$$\mathrm{RTPP} = \int_{\mathbb{R}} E(q\mathbf{r}_{||})dq = \sqrt{\frac{\pi}{4\pi^2\tau}}\sqrt{\frac{1}{D(\mathbf{r}_{||})}} \tag{6}$$

where $\mathbf{r}_{||}$ denotes the direction of maximal diffusion. This measure is known to be a good indicator of restrictive barriers in the axial orientation, and it is related to the mean pore length (Özarslan et al., 2013; Brusini et al., 2015; Boscolo Galazzo et al., 2018).

3. **Return-to-axis probability (RTAP)**:

$$\begin{aligned}\mathrm{RTAP} &= \textstyle\int_{\mathbf{q}\perp\mathbf{r}_{||}} E(\mathbf{q})d\mathbf{q} \\ &= \frac{1}{2\cdot 4\pi^2\tau}\mathcal{G}\left\{D(\mathbf{u})^{-1}\right\}(\mathbf{r}_{||})\end{aligned} \tag{7}$$

where $\mathbf{q}\perp\mathbf{r}_{||}$ is the set of directions perpendicular to $\mathbf{r}_{||}$ and $\mathcal{G}\left\{D(\mathbf{u})^{-1}\right\}(\mathbf{r}_{||})$ is the Funk-Radon Transform (FRT) (Tuch, 2004) of $D(\mathbf{u})^{-1}$ evaluated at $\mathbf{r}_{||}$, the direction of maximum diffusion. The RTAP is an indicator of restrictive barriers in the radial orientation (Özarslan et al., 2013; Zucchelli et al., 2016; Karmacharya et al., 2018).

4. **Apparent Propagator Anisotropy (APA)**: quantifies how much the propagator diverges from the closest isotropic one. For AMURA, we can define:

$$\mathrm{APA}_0 = \sqrt{1 - \frac{4}{\sqrt{\pi}}\frac{\left[C_{0,0}\{(D(\mathbf{u})+D_{\mathrm{AV}})^{-3/2}\}\right]^2}{C_{0,0}\{D(\mathbf{u})^{-3/2}\}\cdot D_{\mathrm{AV}}^{-3/2}}}, \tag{8}$$

where $D_{\mathrm{AV}} = \frac{1}{\sqrt{4\pi}}C_{0,0}\{D(\mathbf{u})\}$. To better distribute the output values in the range [0,1], the APA is transformed by a contrast enhancement function as described in Özarslan et al. (2013).

3. Methods

As previously stated, the information provided by the EAP is expressed in terms of scalar indices or metrics to be usable in practice. In Özarslan et al. (2013), Ning et al. (2015), the authors suggest the use of radial moments, i.e. integrals computed over $P(\mathbf{R})$ and weighted by powers of the radial coordinate. Following a similar rationale, the authors in Tristán-Vega and Aja-Fernández (2021) propose the computation of similar moments over $E(\mathbf{q})$. Indices like RTAP and RTPP can be computed as either line or plane integrals over $\mathbf{R}$ which translate to either plane or line integrals over $\mathbf{q}$. Thus, in Tristán-Vega and Aja-Fernández (2021) the diffusion is characterized in a multishell approach through the computation of moments on either the $\mathbf{R}$ or the $\mathbf{q}$ domain. In this work, we will restrict ourselves to the assumptions of AMURA, specifically the simplified diffusion in Eq. (3) and considering only one acquired shell, i.e., only one b-value is available for the computation of the metrics.

3.1. Generalized moments of $E(\mathbf{q})$

First, we consider those moments over the signal defined in the $\mathbf{q}$ domain.

1. **Full moments:** We define the full moments of $E(\mathbf{q})$ as those computed by integration in the whole 3-D space:

$$\Upsilon^p = \int_{\mathbb{R}^3} q^p E(\mathbf{q})d\mathbf{q}. \tag{9}$$

Note that, with this definition, $\mathrm{RTOP} = Y^0$ and $\mathrm{qMSD} = Y^2$ ($\mathbf{q}$–space mean-squared-displacement Ning et al., 2015). By using the simplification in Eq. (3), we can write Eq. (9) in spherical coordinates and integrate with respect to the radial component q:

$$\begin{aligned}Y^p &= \int_0^\infty \int_{\mathcal{S}} q^{2+p}\exp(-4\pi^2\tau q^2\cdot D(\mathbf{u}))\ d\mathbf{u}\ dq \\ &= \frac{1}{2}\Gamma\left(\frac{3+p}{2}\right)\frac{1}{(4\pi^2\tau)^{\frac{3+p}{2}}}\int_{\mathcal{S}} D(\mathbf{u})^{-\frac{3+p}{2}}d\mathbf{u},\end{aligned} \tag{10}$$

the integral being convergent only if $p > -3$. Using the zeroth-order coefficient of a SH expansion to calculate the integral over the surface of the unit sphere $\mathcal{S}$, we can write:

$$Y^p = \Gamma\left(\frac{3+p}{2}\right)\frac{\sqrt{\pi}}{(4\pi^2\tau)^{\frac{3+p}{2}}}C_{0,0}\left\{D(\mathbf{u})^{-\frac{3+p}{2}}\right\},\quad p > -3. \tag{11}$$

The units of the full moment Y^p are $[\mathrm{mm}^{-p-3}]$.

2. **Axial moments:** We define the axial moments as those computed as a line integral along a given direction:

$$Y_{||}^p = \int_{\mathbb{R}} q^p E(q\mathbf{r}_{||})dq, \tag{12}$$

where $\mathbf{r}_{||}$ denotes the direction of maximal diffusion. With this definition, $\mathrm{RTPP} = Y_{||}^0$. Once more, we can use the simplification in Eq. (3) and therefore:

$$\begin{aligned}Y_{||}^p &= \int_{-\infty}^{\infty} q^p\exp(-4\pi^2\tau q^2 D(\mathbf{r}_{||}))dq \\ &= \frac{1}{(4\pi^2\tau)^{\frac{1+p}{2}}}\Gamma\left(\frac{1+p}{2}\right)D(\mathbf{r}_{||})^{-\frac{1+p}{2}},\quad p > -1,\end{aligned} \tag{13}$$

where $D(\mathbf{r}_{||})$ is the value of the diffusion signal $D(\mathbf{q})$ at the maximum diffusion direction $\mathbf{r}_{||}$. Again, the condition $p > -1$ ensures the convergence of the integral. The axial moment $Y_{||}^p$ is measured in $[\mathrm{mm}^{-p-1}]$.

3. **Planar moments:** We define the planar moments as those computed as surface integrals in a plane perpendicular to a desired direction containing the origin:

$$Y_{\perp}^p = \int_{\mathbf{q}\perp\mathbf{r}_{||}} q^p E(\mathbf{q})d\mathbf{q}, \tag{14}$$

where $\mathbf{q}\perp\mathbf{r}_{||}$ is the set of directions perpendicular to $\mathbf{r}_{||}$ (the one with maximal diffusion). With this definition, $\mathrm{RTAP} = Y_{\perp}^0$. In order to simplify the equation, we use again the simplification in Eq. (3). Let θ be the angle that parameterizes the equator perpendicular to the maximum diffusion direction, $\{\mathbf{u}_{\perp}(\theta), \theta\in[0,2\pi)\} \equiv \{\mathbf{u} : \mathbf{u}\perp\mathbf{r}_{||}, \|\mathbf{u}\| = 1\}$, and $D(\mathbf{u}_{\perp}(\theta))$ the diffusion signal at that equator. Since $D(\mathbf{u}_{\perp}(\theta))$ does not depend on the radial component, the previous integral can be developed into:

$$\begin{aligned}Y_{\perp}^p &= \int_0^\infty \int_0^{2\pi} \exp(-4\pi^2\tau q^2 D(\mathbf{u}_{\perp}(\theta)))\ q^{p+1}\ d\theta\ dq \\ &= \frac{1}{2}\frac{1}{(4\pi^2\tau)^{\frac{p+2}{2}}}\Gamma\left(\frac{2+p}{2}\right)\int_0^{2\pi} D(\mathbf{u}_{\perp}(\theta))^{-\frac{2+p}{2}}d\theta.\end{aligned} \tag{15}$$

By assuming $p > -2$ we can guarantee the integral is convergent. The FRT operator allows a more compact notation:

$$Y_{\perp}^p = \frac{1}{2}\frac{1}{(4\pi^2\tau)^{\frac{p+2}{2}}}\Gamma\left(\frac{2+p}{2}\right)\mathcal{G}\left\{D(\mathbf{u})^{-\frac{2+p}{2}}\right\}(\mathbf{r}_{||}),\quad p > -2. \tag{16}$$

The units of the planar moment $Y_{\perp}^p$ are $[\mathrm{mm}^{-p-2}]$.

3.2. Generalized (full) moments of $P(\mathbf{R})$

A closed form expression of $P(\mathbf{R})$ cannot be attained in the general case from the mono-exponential model of $E(\mathbf{q})$. Even so,

Table 1
Survey of the moments of $E(\mathbf{q})$ and $P(\mathbf{R})$ calculated with AMURA.

Measure	Numerical Implementation
Full moments of $E(\mathbf{q})$	$Y^p = \Gamma\left(\frac{3+p}{2}\right)\frac{\sqrt{\pi}}{(4\pi^2\tau)^{\frac{3+p}{2}}} C_{0,0}\left\{D(\mathbf{u})^{-\frac{3+p}{2}}\right\}, \quad p > -3$
Axial moments of $E(\mathbf{q})$	$Y^p_{\|\|} = \frac{1}{(4\pi^2\tau)^{\frac{1+p}{2}}}\Gamma\left(\frac{1+p}{2}\right) D(\mathbf{r}_{\|\|})^{-\frac{1+p}{2}}, \quad p > -1$
Planar moments of $E(\mathbf{q})$	$Y^p_{\perp} = \frac{1}{2}\frac{1}{(4\pi^2\tau)^{\frac{p+2}{2}}}\Gamma\left(\frac{2+p}{2}\right)\mathcal{G}\left\{D(\mathbf{u})^{-\frac{2+p}{2}}\right\}(\mathbf{r}_{\|\|}), \quad p > -2$
Full moments of $P(\mathbf{R})$	$\upsilon^p = \frac{\Gamma\left(\frac{p+3}{2}\right)}{q^p\pi^{p+1}} C_{0,0}\left\{D^{\frac{p}{2}}(\mathbf{u})\right\}, \quad p > -3$

full moments analogous to those defined for $E(\mathbf{q})$ can be explicitly computed. In precise terms, we define the pth full moment of $P(\mathbf{R})$ as:

$$\upsilon^p = \int_{\mathbb{R}^3} R^p P(\mathbf{R}) d\mathbf{R}. \tag{17}$$

where $R = |\mathbf{R}|$. Using spherical coordinates, we can rewrite it to:

$$\upsilon^p = \int_{\mathcal{S}} \left(\int_0^{\infty} R^{p+2} P(R\mathbf{r}) dR \right) d\mathbf{r}, \quad p > -3, \tag{18}$$

where $\mathbf{r} \in \mathcal{S}$ is a unitary direction in space and, therefore, $\mathbf{R} = R\mathbf{r}$ and $|\mathbf{r}| = 1$. If we consider the mono-exponential model in Eq. (3) we can solve the integral, see Appendix A:

$$\upsilon^p = \frac{\Gamma\left(\frac{p+3}{2}\right)}{2q^p\pi^{p+\frac{3}{2}}} \int_{\mathcal{S}} D^{\frac{p}{2}}(\mathbf{u}) d\mathbf{u}, \quad p > -3. \tag{19}$$

Following the Eq. (19), $\mathrm{MSD} = \upsilon^2$. Using the zeroth-order coefficient of a SH expansion to calculate the integral over the surface of the unit sphere $\mathcal{S}$, we can write:

$$\upsilon^p = \frac{\Gamma\left(\frac{p+3}{2}\right)}{q^p\pi^{p+1}} C_{0,0}\left\{D^{\frac{p}{2}}(\mathbf{u})\right\}. \tag{20}$$

The full moment υ^p is given in $[\mathrm{mm}^p]$.

3.3. Survey

An overview of the different moments proposed in this section, together with their specific numerical implementations, is presented in Table 1. In addition, Appendix B provides the analogous expressions for DT representation.

4. Materials

In order to test the proposed measures the following datasets were used:

- **Human Connectome Project (HCP) MGH database** (Fan et al., 2016; Moeller et al., 2021)[1]: specifically volumes MGH1007, MGH1010, MGH1016, MGH1026 and MGH1030, acquired on a Siemens 3T Connectom scanner (Siemens, Erlangen, Germany) equipped with a custom-made 64-channel head coil and gradient coil capable of producing a maximum gradient strength at 300 mT/m. The data were acquired with a mono-polar Stejskal–Tanner pulsed gradient spin-echo echo planar imaging (EPI) with (repetition time/time echo) TR/TE = 8800/57 ms and accelerated with the Generalized Autocalibrating Partially Parallel Acquisition (GRAPPA) protocol at phase partial Fourier 6/8. The acquisition protocol included four b-values at $\{1000, 3000, 5000, 10,000\}$ s/mm^2 sampled at 64, 64, 128 and 256 directions respectively, 40 non-diffusion acquisitions at $b = 0$, voxel resolution $1.5 \times 1.5 \times 1.5$ mm^3, pixel bandwidth 1984 Hz/pixel, acquisition matrix 140×140 with 96 slices covering each volume, and pulse separation time/diffusion gradients length $\Delta/\delta = 21.8/12.9$ ms.
- **Human Connectome Project (HCP) WU-Minn test-retest database:** (Van Essen et al., 2013; Moeller et al., 2021): Thirty-seven subjects were used after excluding seven cases from the database due to incompatibilities between test and retest acquisitions (excluded volumes: 135528, 137128, 151526, 169343, 179548, 192439, 601127, 660951). All subjects were scanned with a customized Siemens 3T Connectome Skyra scanner (Siemens, Erlangen, Germany) equipped with a 32-channel head coil and gradient coil with a maximum gradient strength at 100 mT/m. The data were acquired using the multiband approach with a multiband factor of 3, TR/TE = 5520/89.5 ms. The acquisition protocol included three b-values at $\{1000, 2000, 3000\}$ s/mm^2, each shell sampled in 90 non-collinear directions, 18 repetitions of the baseline acquisition ($b = 0$), voxel resolution $1.25 \times 1.25 \times 1.25$ mm^3, pixel bandwidth 1490 Hz/pixel, 140 slices covering each volume, and pulse separation time/diffusion gradients length $\Delta/\delta = 43/10.6$ ms.
- **Multishell data acquired at CUBRIC (CBR)**[2]: 14 healthy volunteers scanned on a 3T Siemens Prisma scanner (maximum gradient strength at 80 mT/m) with a pulsed-gradient spin-echo (PGSE) sequence. Three shells were acquired at $b = \{1200, 3000, 5000\}$ s/mm^2 with 60 directions per value. The voxel resolution is $1.5\times$ 1.5 $\times$ 1.5 mm. Other acquisition parameters are: TE=80 ms, TR=4500 ms, $\Delta/\delta = 38.3/19.5$ ms, parallel imaging acquisition (GRAPPA2) with sum of squares combination and 32 channels.
- **Episodic Migraine Database (EMDb)**: as described in Planchuelo-Gómez et al. (2020a), Planchuelo-Gomez et al. (2020). For this paper we will consider a total of 50 healthy controls (HCs) at the age of 36.1 $\pm$ 13.2 (39F, 11M) and 51 patients with Episodic Migraine (EM) at the age of 36.6 $\pm$ 7.9 (44F, 7M) and duration of migraine 13.1y $\pm$ 10.5y. The study was approved by the Ethics Committee of the Hospital Clínico Universitario de Valladolid (PI: 14–197). The inclusion criteria of EM follow the International Classification of Headache Disorders guidelines (Zhang et al., 2016). MRI acquisition was performed with a Philips Achieva 3 T MRI unit (Philips Healthcare, Best, The Netherlands), using a 32-channel head coil in the MRI facility at the Universidad de Valladolid (Valladolid, Spain). The parameters of the diffusion-weighted acquisition are as follows: TR/TE = 9000/86 ms, flip angle = 90°, single-shell acquisition with 61 gradient directions and $b = 1000$ s/mm^2, one baseline volume, 128×128 matrix size, spatial resolution of $2 \times 2 \times 2$ mm^3 and 66 slices that cover the whole brain. Both T1 and diffusion-weighted data were collected between May 2014 and July 2018 in a unique MRI session, starting with the T1 scan. For a single subject, the time for both scans was approximately 18 min. The data were preprocessed following a standard pipeline: denoising, correction for eddy currents and motion and correction for B1 field inhomogeneity, and Gibbs ringing artifact. The MRtrix software (Tournier et al., 2019) was employed to carry out these steps.

[1] Data obtained from the Human Connectome Project (HCP) database (ida.loni.usc.edu/login.jsp). The HCP project (Principal Investigators: Bruce Rosen, M.D., Ph.D., Martinos Center at Massachusetts General Hospital; Arthur W. Toga, Ph.D., University of Southern California, Van J. Weeden, MD, Martinos Center at Massachusetts General Hospital) is supported by the National Institute of Dental and Craniofacial Research (NIDCR), the National Institute of Mental Health (NIMH) and the National Institute of Neurological Disorders and Stroke (NINDS). HCP is the result of efforts of co-investigators from the University of Southern California, Martinos Center for Biomedical Imaging at Massachusetts General Hospital (MGH), Washington University, and the University of Minnesota.

[2] www.cardiff.ac.uk/cardiff-university-brain-research-imaging-centre/research/projects/cross-scanner-and-cross-protocol-diffusion-MRI-data-harmonisation

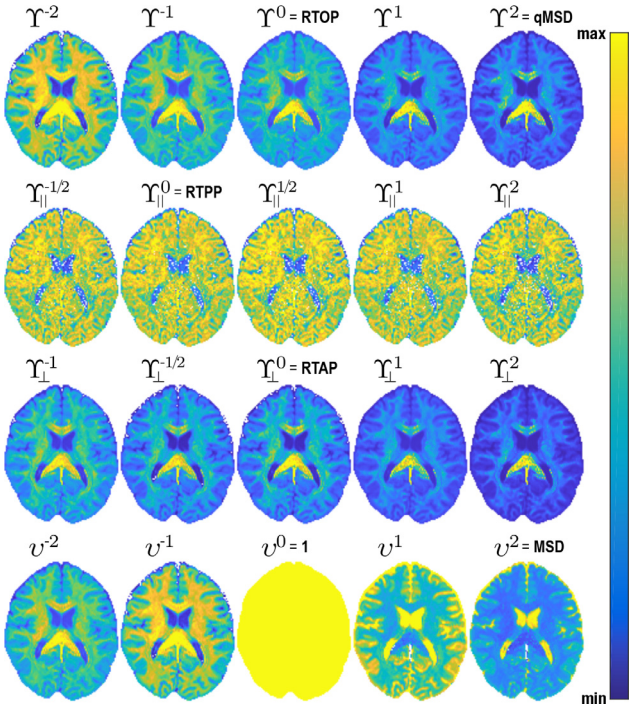

Fig. 1. Moments of different kinds for different orders p computed over the composite attenuation signal over subject HCP MGH1007. Each moment has been normalized to its own range for visualization purposes. Top to bottom: full moments (Y^p); axial moments for the maximum diffusion direction ($Y_{||}^p$); planar moments for the maximum diffusion direction ($Y_{\perp}^p$) and full moments of the EAP (υ^p). These indices include RTOP, qMSD, RTPP, RTAP and MSD.

A whole brain mask for each subject was also calculated from data.

5. Experiments and results

5.1. Setting-up of the experiments

AMURA and MiSFIT measures were calculated using the dMRI-Lab[3] toolbox and MATLAB 2020a. As explained above, AMURA measures rely on the expansion of spherical functions at a given shell in the basis of SH. Even SH orders up to 6 were fitted with a Laplace-Beltrami penalty $\lambda = 0.006$. The direction of maximum diffusion $\mathbf{r}_{||}$ was computed as the principal eigenvector of the diffusion tensor calculated from the same data set as the AMURA. The FRT was numerically computed as described in Descoteaux et al. (2007): the spherical function $-D(\mathbf{u})-$ was first spanned in the basis of SH up to the desired order L; then, we exploited the property of SH being eigenfunctions for the FRT by applying constant factors –FRT eigenvalues– to the SH coefficients. As a result, we got the SH coefficients of the analytically computed FRT of the original signal, which could now be evaluated for any orientation at will (and, in particular, for $\mathbf{r}_{||}$).

5.2. Behavior of moments for varying orders

A preliminary visual assessment of the different metrics was performed using one single slice from the HCP volume MGH1007. The proposed measures were calculated using a single shell at $b = 3000$ s/mm^2. Figure 1 provides a qualitative insight in the behavior of moments computed in the $\mathbf{q}$ and $\mathbf{R}$ domains. Each kind of moment (full, axial, or planar) admits a different range of variation for its order depending on the convergence of the corresponding integral. Accordingly, we have probed a range including inverse (negative), positive and fractional orders in all cases. Since their ranges of variation are very different from each other depending on the order and the kind of moment, all the slices shown have been min-max normalized.

First of all, note that the popular RTOP, RTPP and RTAP could be already calculated with the original formulation of AMURA. Here, we can see them as special values of the considered moments. Full moments Y^p, for instance, show a different range of quantification of the variation of the white matter as a function of the order p. Axial moments $Y_{||}^p$ result in very noisy maps with a reduced anatomical coherence, an effect that can also be seen in RTPP, even when calculated with more shells and more advanced methods (Tristán-Vega and Aja-Fernández, 2021). These moments are especially sensitive to the signal-to-noise ratio (SNR). Planar moments $Y_{\perp}^p$, on the other hand, exhibit a behavior very similar to the full moments. Anatomical structures in white matter are distinguishable even for negative and not even orders. Finally, moments of $P(\mathbf{R})$, υ^p, show a behavior different to the previous ones. Note that $\upsilon^0 = 1$ since it is the integral of the whole EAP, which represents a PDF. On the other hand, note that, from an implementation point of view, υ^p are defined as positive powers of $D(\mathbf{u})$, while the moments of $E(\mathbf{q})$ are defined over negative powers, hence the visual differences.

Next, we will focus in the values of the different moments in one particular area of the brain, the CC. Different AMURA metrics were calculated on HCP volumes MGH1016, MGH1026 and MGH1030 using a single shell at $b = 5000$ s/mm^2 for higher contrast. The CC was extracted using the registration of the subject's FA (calculated at $b = 1000$ s/mm^2) to a common template using the FSL 6.0.4 (Analysis Group, FMRIB, Oxford, UK.; https://fsl.fmrib.ox.ac.uk/fsl/fslwiki ; Smith et al., 2004), applying the JHU WM atlas (Mori et al., 2005) and then averaging the measures over three subjects. Specifically, we linearly registered the FA to the template FMRIB58 (a high-resolution FA average over 58 subjects) with a voxel resolution of $1 \times 1 \times 1$ mm^3 (Jenkinson and Smith, 2001; Jenkinson et al., 2002) using twelve degrees of freedom and normalized correlation as the cost function. We then applied a nonlinear registration procedure to correct the matching of the subject's FA to the template. Once the FAs were registered to the common space, we warped the AMURA based measures to the standard space using trilinear interpolation. The values of the different metrics over the CC are depicted in Fig. 2 for a single sagittal view. Once more, the metrics have been min-max normalized in order to show a similar range of values. A 3D rendering of the CC is shown for reference.

According to previous analyses (Aboitiz et al., 1992; 2003), the CC presents different fiber structure configurations for the three different parts: the genu CC (GCC), the body CC (BCC) and the splenium CC (SCC). The different regions have a wide variety of diffusion properties, distributed in an uneven manner along this structure, as reflected in the scheme in Fig. 2-left, extracted from Aboitiz et al. (2003). In Fig. 2, those moments based on $E(\mathbf{q})$ reflect the differences in the diffusion properties for the different parts of the CC. This difference is more noticeable with higher order moments, like Y^2, $Y_{||}^2$ and $Y_{\perp}^2$. On the contrary, this effect is not reflected on the moments of $P(\mathbf{R})$.

5.3. DT vs. AMURA

Some of the moments presented in this study can also be implemented using the DT approach, as described in Appendix B. In this section we will show how AMURA provides distinct representations than DT does, which will potentially lead to markers more

[3] www.lpi.tel.uva.es/dmrilab

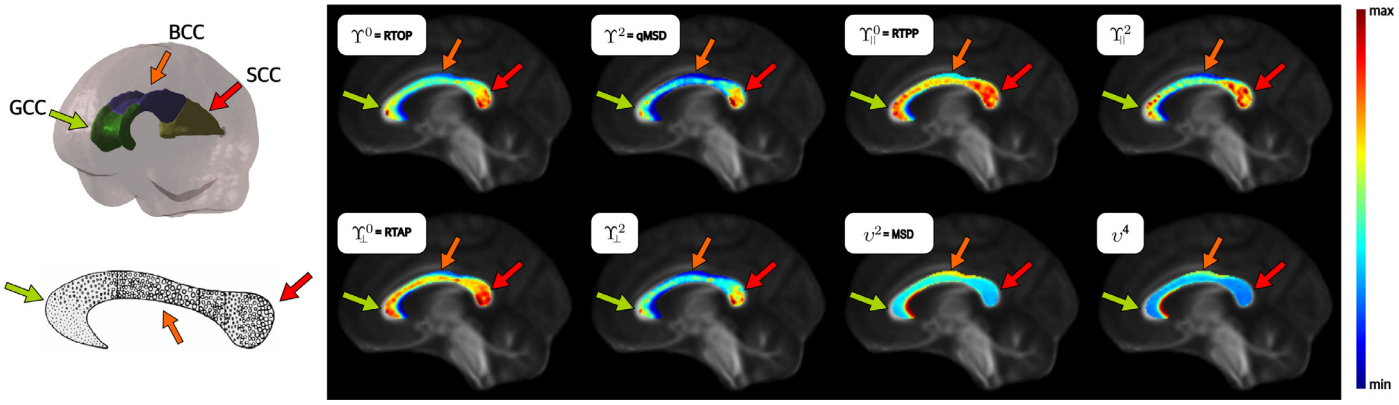

Fig. 2. Values of different moments calculated with AMURA on the CC for the average of volumes MGH1016, MGH1026 and MGH1030 using a single-shell at $b = 5000$ s/mm^2 in the standard space, sagittal view. The values of the measures are displayed over the FA for reference. Scheme of the fiber distribution in the corpus callosum extracted from Aboitiz et al. (2003) with marked regions: the genu corpus callosum (GCC), the body corpus callosum (BCC) and the splenium corpus callosum (SCC).

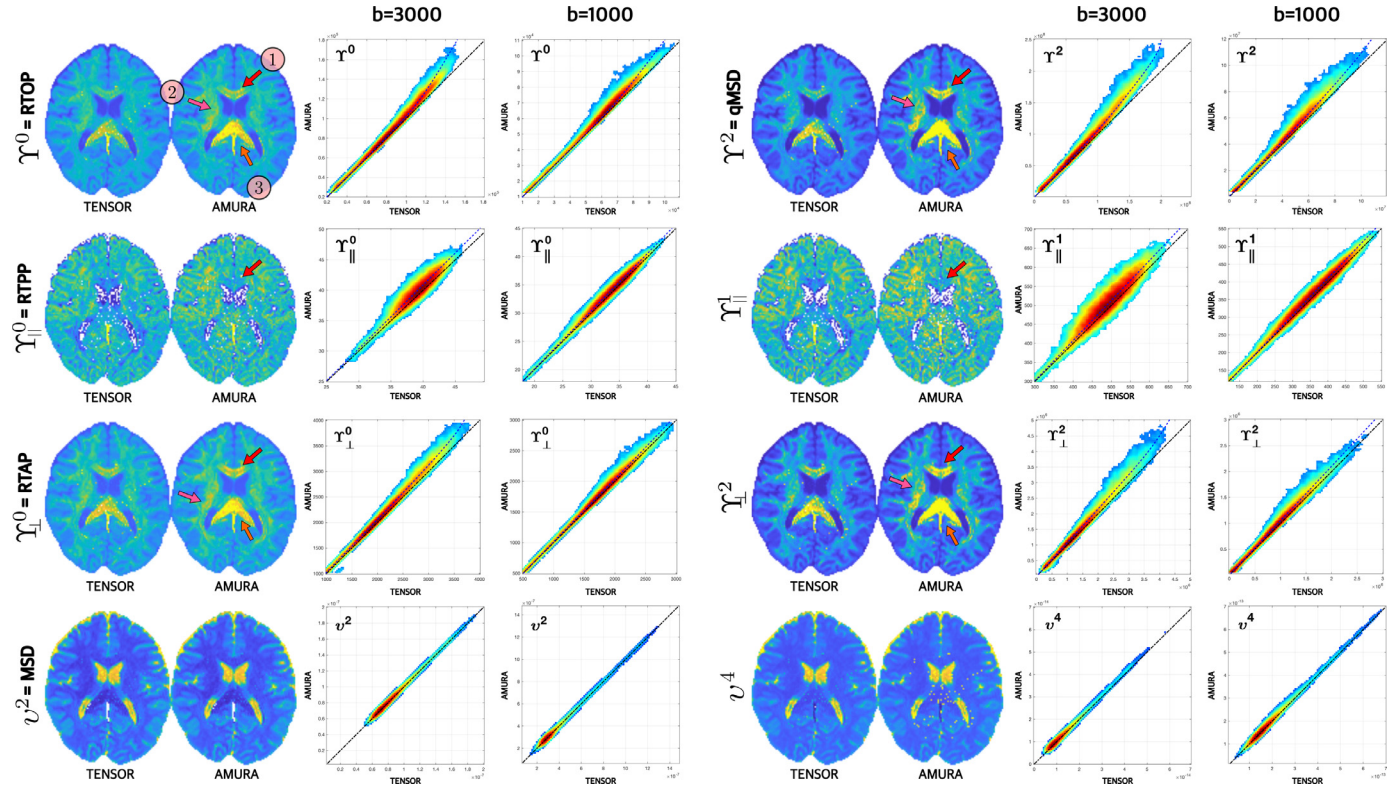

Fig. 3. Comparison of scalar measurements computed with either the DT (left) or AMURA (right) over subject HCP MGH1007 at $b = 3000$ s/mm^2. The same scale is used for both two approaches in all cases. Joint 2-D histograms for the comparison at $b = 3000$ s/mm^2 and $b = 1000$ s/mm^2 are shown in each case. Arrows highlight prominent differences between the DT and AMURA: (1) genu of corpus callosum, (2) centrum semiovale and (3) splenium of the corpus callosum.

sensitive to anatomical changes. Different measures were calculated on volume MGH1007 using a single shell at two different b-values: $b = 1000$ s/mm^2 and $b = 3000$ s/mm^2. For the sake of visual comparison, Fig. 3 shows respective slices of different moments calculated with DT and with AMURA for $b = 3000$ s/mm^2 with identical scaling, so that they can be directly compared, together with the voxel-wise joint 2-D histograms for both considered shells. While the structure of the anatomical maps look quite similar with the two approaches, and their ends of scale are also coherent, AMURA systematically shows greater values than the DT at the corpus callosum (CC, 1 and 3) and the centrum semiovale (2).

The centrum semiovale is a region with a complex fiber configuration in terms of crossing fibers: there is a conjunction of structures with different alignment, like anterior-posterior (cingulum and superior longitudinal fasciculus), left-right (corpus callosum) and superior-inferior (corticospinal tract). It is known to be an area prone to produce false positives in tractography (Knösche et al., 2015). Thus, the adjustment of a Gaussian model (like the DT) will be subject to underestimation of the diffusion in this region. A more general model like AMURA, despite also being based on an mono-exponential decay, will produce higher values, more coherent with actual structures.

The divergence of values in the CC is explained by a different effect. In that area, the fibers follow a similar main direction, with high anisotropy. However, the underlying structure is a bit more complex than most tracts in white matter, since it shows a greater curvature. The resolution of the DMRI data is not enough to dis-

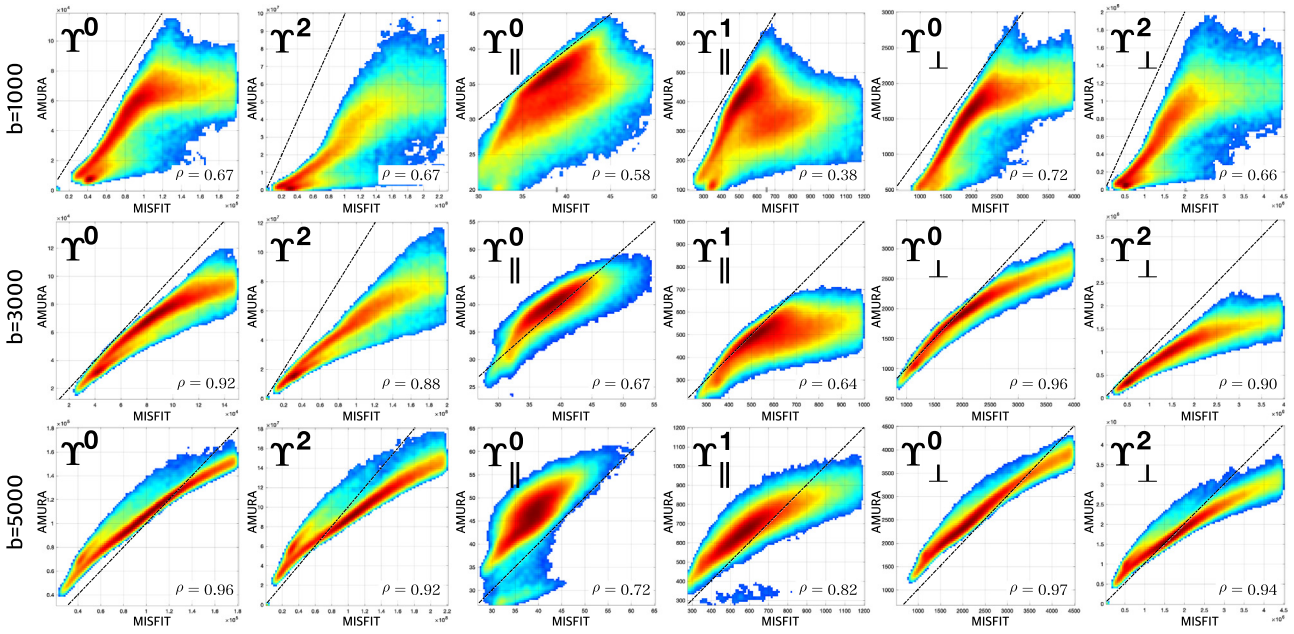

Fig. 4. Comparison of the moments of $E(\mathbf{q})$ computed with AMURA and MiSFIT. A joint 2-D histogram is shown in each case, together with the respective Pearson's correlation coefficient, for quantitative assessment. AMURA is calculated using a single shell with the b-value specified on the left side of each row. MiSFIT is calculated using three shells.

criminate this subvoxel curvature, especially in approaches like DT, where only one predominant direction is considered. Actually, in Knösche et al. (2015), the authors report analogous problems with tractography in the CC due to this same effect. In addition, full and planar moments calculated with the DT are an inverse function of the smallest eigenvalues (see Appendix B). In those areas with higher anisotropy, like the CC, where the second and third eigenvalues are particularly low, the effect of noise could bias them to higher values, a well-known effect in the DT when estimated using a least-squares approach (Farrell et al., 2007; Aja-Fernández et al., 2008; Tristán-Vega et al., 2012). As a consequence, metrics like RTOP and RTAP will show lower values in those areas when calculated with the DT.

On the other hand, note that the moments based on $P(\mathbf{R})$ show almost no difference between both implementations.

Paying attention to the voxel-wise joint 2-D histograms, the DT approach consistently shows an underestimation of the greater values when compared to AMURA, specifically in the full and planar moments of $E(\mathbf{q})$. This mismatch is more significant at $b = 3000$ s/mm^2, whereas for $b = 1000$ s/mm^2 the differences remain, but to a smaller degree. The histograms show that DT and AMURA diverge when the b-value grows. On the other hand, values for the moments of $P(\mathbf{R})$ are almost the same for both implementations. This effect, once again, could be easily explained by the fact that υ^p is calculated over positive powers of $D(\mathbf{u})$.

5.4. Comparison with multishell metrics

The *apparent* moments calculated with AMURA are now compared to the same *actual* moments calculated with a multishell approach where the radial information of $\mathbf{q}$ is taken into account, specifically Micro-Structure-adaptive convolution kernels and dual Fourier domains Integral Transforms (MiSFIT) (Tristán-Vega and Aja-Fernández, 2021). For both methods, volume MGH1010 is considered. AMURA is calculated independently for three separated shells at $b = \{1000, 3000, 5000\}$ s/mm^2 while MiSFIT is calculated using the three available shells at once. Figure 4 shows the voxel-wise joint 2-D histogram for the moments of $E(\mathbf{q})$. For each moment, Pearson's correlation coefficient between both methods is calculated. There are clearly differences, since both methods are based on very different initial assumptions. However, for higher b-values, full and planar moments of the $E(\mathbf{q})$ show a very strong correlation between the estimation with AMURA using only one shell and the multishell calculation given by MiSFIT. In some cases, that correlation exceeds the 90%, which basically means that those methods are measuring very similar information. However, the mapping of both methods is not linear, with AMURA showing a reduced contrast when compared to MiSFIT, especially for the highest values. Axial moments are the ones showing more differences with greater dispersion.

All the measures show a low correlation when AMURA is calculated at $b = 1000$ s/mm^2, which is expected, since the underlying features measured by the estimated moments are better visible at higher b-values. This experiment shows that the best performance of AMURA is achieved for higher b-values, where the correlation with multishell methods is stronger. In addition, the correlation seems weaker when higher order moments are considered.

Figure 5 shows the voxel-wise joint 2-D histogram for the moments of $P(\mathbf{R})$. Results here are weaker than the previous case. This, once more, shows the inability of AMURA to properly estimate the moments of $P(\mathbf{R})$. While the moments of $E(\mathbf{q})$ could provide equivalent information when calculated from a single shell, for a proper estimation of the moments of $P(\mathbf{R})$ experimental results points to the need of multishell information.

5.5. Variability of measures depending on the b-value

Next, since AMURA provides *apparent* measures at a given shell, we tested the dependency of different moments on the b-value. To put this to the test, the variability with the b-value is probed using five whole volumes from the CBR data with the following procedure: Each AMURA moment was calculated at $b = 3000$ s/mm^2 on the white matter and outliers are removed. Then, that moment was clustered in fivedifferent groups inside using k-means algorithm. Each voxel in the white matter was assigned to the closest cluster using the minimum distance. As a result, the whole volume

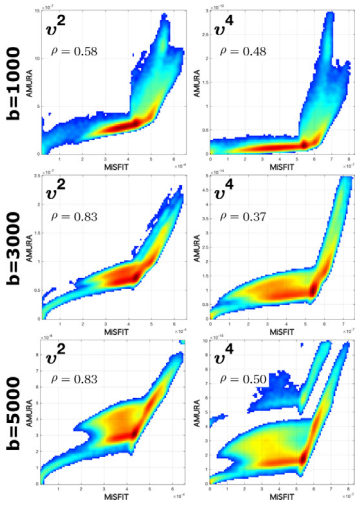

Fig. 5. Comparison of the moments of $P(\mathbf{R})$ computed with AMURA and MiSFIT. A joint 2-D histogram is shown in each case, together with the respective Pearson's correlation coefficient, for quantitative assessment. AMURA is calculated using a single shell with the b-value specified on the left side of each row. MiSFIT is calculated using three shells.

was divided into six different region-of-interests (ROIs) of similar value of the moment at $b = 3000$ s/mm^2. Then, the variability with the b-value was probed by computing the different AMURA measures with each of the available shells at $b = 1200$ s/mm^2, $b = 3000$ s/mm^2, or $b = 5000$ s/mm^2. All the proposed measures were computed for each considered case, and the median value inside each of the six clusters was calculated and depicted in Fig. 6.

All the considered measures show an indubitable dependence on the b-value. There is a monotonical behavior of each cluster for full and planar moments where the value grows with b. However, the separation between clusters remains for different b-values. This suggests that differences detected by these measures can be detected when using different shells This is not exactly the case for axial moments, where the cluster with lowest value shows a different behavior, decreasing for $b = 3000$ s/mm^2. This is motivated by the very noisy nature of this cluster, see for instance Fig. 1. The lowest values of the axial moments are prone to more variability than higher values.

5.6. Test-retest reproducibility analysis

Next, we evaluate the variability of the moments of AMURA using the HCP WU-Minn test-retest database. This database facilitates subsampling of the data by choosing the first k ($k < N$) diffusion gradient directions out of N samples, so that we subsampled the original data (90 directions) to 45, 30 and 15 gradients subsets per single-shell. To improve the SNR of the baseline (i.e. the non-diffusion weighted data), we averaged all together 18 non-diffusion weighted volumes. We estimated then AMURA measures for each subject, b-value and all four different numbers of gradient directions (i.e. 90, 45, 30 and 15 samples per each shell). We also estimated DTs from $b = 1000$ s/mm^2 data using the FSL (Smith et al., 2004). Hither, the same sampling coverage was employed as the one used for AMURA measures. We retrieved then the FA, full/axial/planar moments of $E(\mathbf{q})$ and full moments of the diffusion propagator $P(\mathbf{R})$ directly from tensor eigenvalues estimated at each data subsampling level. The FA calculated from fully-sampled data served for the two-step registration process of each subject to the common space as mentioned before. Similarly, we warped all AMURA and DTI based measures to the standard space using trilinear interpolation. The coefficient of variation (CV) is defined in the standard space for each subject, measure and subsampling ratio as the sample standard deviation across two sessions (i.e. test and retest) divided by the sample mean across sessions, and eventually multiplied by 100 to get the percentage score

$$\mathrm{CV}_s(\mathbf{x}) = \frac{\text{sample std. dev}_s(\mathbf{x})}{\text{sample mean}_s(\mathbf{x})} \cdot 100\ [\%] \quad \text{for} \quad s = 1, \ldots, S, \quad (21)$$

where $\mathrm{CV}_s(\mathbf{x})$ is a position dependent ($\mathbf{x}$-dependent) CV of a measure under a specified acquistion scenario (i.e. b-value, number of gradient directions) for subject s and S is the number of subjects used for the experiment (i.e. $S = 37$ for the HCP WuMinn database). The final CV is aggregated across all subjects using median operation for each measure, acquisition scenario and spatial position $\mathbf{x}$ separately:

$$\mathrm{CV}(\mathbf{x}) = \underset{s=1,\ldots,S}{\text{median}}\ \mathrm{CV}_s(\mathbf{x}). \quad (22)$$

Results of two reproducibility experiments are depicted in Figs. 7, 8 and 9. In the former experiment, we compare median CV maps of the moments of $E(\mathbf{q})$ and diffusion propagator $P(\mathbf{R})$ retrieved from a single-shell diffusion MR data with the DT at $b = 1000$ s/mm^2 and AMURA separately for $b = 1000, 2000$ and 3000 s/mm^2, all using 30 gradient directions. Figure 7 presents the median CV, $\mathrm{CV}(\mathbf{x})$, calculated over all thirty-seven subjects from the HCP WU-Minn test-retest database in the standard space (slice 85), including both the DT and AMURA. The smallest CV amongst all cases is observed for the zeroth-order axial moment of $E(\mathbf{q})$ (RTPP) and the second-order full moment of diffusion propagator $P(\mathbf{R})$ (MSD), while the highest one is noticeable for the second-order full and planar moments (qMSD, $Y_\perp^2$), especially in highly anisotropic regions such as the corpus callosum (genu and splenium), fornix and anterior/posterior limb of the internal capsule (see the arrows in Fig. 7). The CVs for the AMURA at $b = 1000$ s/mm^2 are comparable to those obtained from the DT, but in the former case, the CV is decreased with the higher b-value regime. Importantly, the CV increases with the positive moment's order consistently for all types of moments of $E(\mathbf{q})$ and $P(\mathbf{R})$.

The latter reproducibility experiment matches the median CV maps and their histograms determined with the DT and AMURA under the varying number of diffusion gradients used to calculate the moments of $E(\mathbf{q})$ and $P(\mathbf{R})$ starting from fully-sampled volumes (90 directions per shell) and then subsampled data to 45 and 15 directions, respectively. Here, we contrast AMURA measures calculated at $b = 3000$ s/mm^2 to DT-based ones from $b = 1000$ s/mm^2 (see Fig. 8). Generally, both the AMURA and DT exhibit robustness due to a decreasing number of diffusion gradient directions. However, we can observe an increase in the CV obtained from the DT with 15 gradient directions, which is notably prominent in the region of the SCC, including full Y^p and planar $Y_\perp^p$ moments. Notice we modified the scale in Fig. 8 to delineate the differences between the methods across varying number of gradients. Next, for each measure retrieved with DTI at $b = 1000$ s/mm^2 and AMURA at $b = 1000$ and 3000 s/mm^2, we calculated the histogram from the median CV map aggregated from 37 subjects, $\mathrm{CV}(\mathbf{x})$, over the brain area of a representative slice (slice 85). We applied then a kernel density estimation method with a bandwidth selection using Scott's Rule to generate smoothly varying curves and put them together for each measure in Fig. 9. In both the AMURA and DT, we observe shifts in histogram peaks towards higher median CV value, especially once the number of gradients reduce to 15. Nonetheless, the changes in estimated density plots are consistent across all evaluated measures and acquisition scenarios with the advantage of AMURA-based measures under a higher b-value.

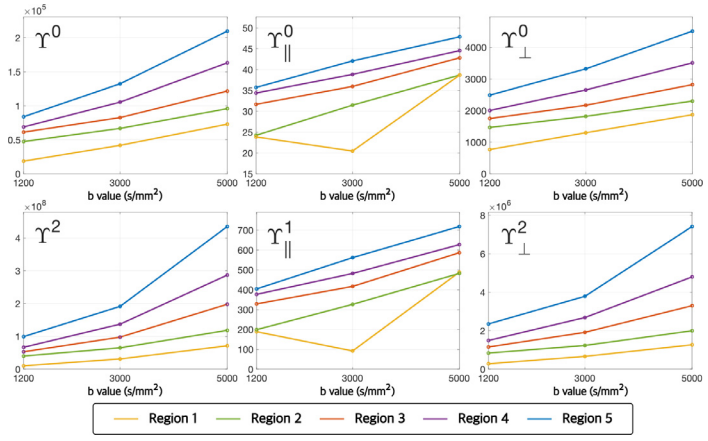

Fig. 6. Evolution of the proposed measures with the b-value using data acquired with a 3T Prisma scanner (CBR dataset). The volume has been clustered in five different sets (for each metric at $b = 3000$ s/mm^2) and the median of each set is shown. Each color represents the median value inside each ROI (1 to 5).

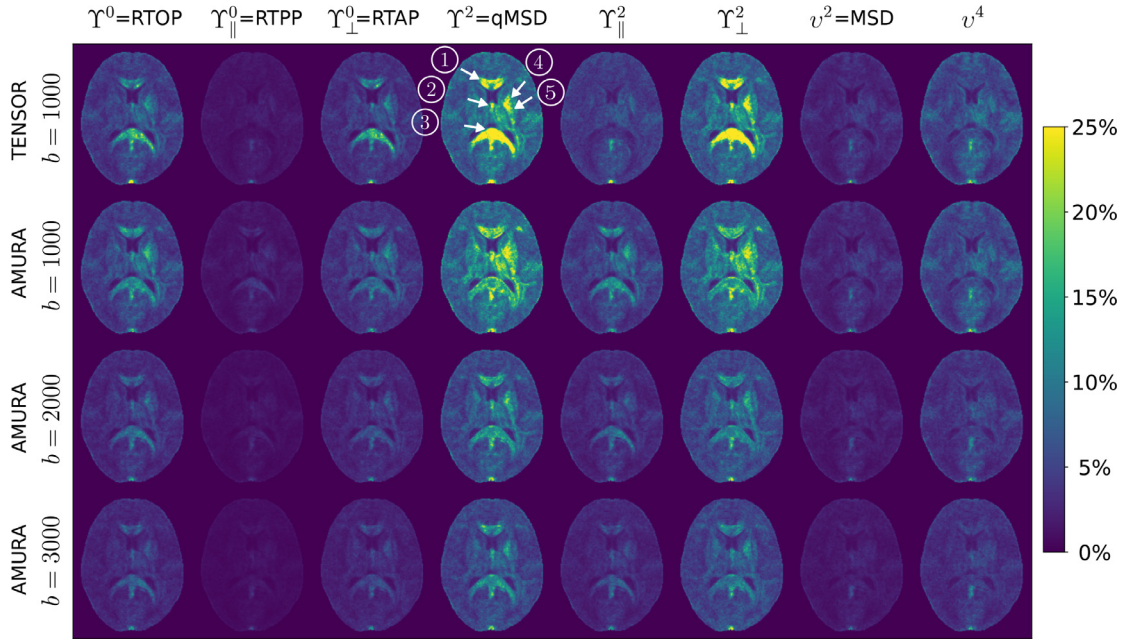

Fig. 7. Median CV maps (defined in %), CV($\mathbf{x}$), of the moments of $E(\mathbf{q})$ and $P(\mathbf{R})$ in the standard space calculated across thirty-seven subjects from the HCP WU-Minn test-retest database. The moments were retrieved from single-shell data at $b = 1000$ s/mm^2 (DT; top) and separately for $b = 1000, 2000$ and 3000 s/mm^2 under the AMURA framework, all using 30 gradient directions per a single-shell. The arrows show the following WM regions: (1) genu of corpus callosum, (2) fornix, (3) splenium of the corpus callosum, (4) left anterior limb of the internal capsule and (5) left posterior limb of the internal capsule.

5.7. Clinical data: Episodic migraine

Finally, in order to test the capability of the new measures to be used in clinical studies, we have selected a very specific pathology, the EM, in which differences in the white matter are particularly hard to find, compared to other frequently assessed disorders such as Alzheimer's disease or schizophrenia. Details about the nature and etiology of migraine can be found elsewhere (Katsarava et al., 2012; Zhang et al., 2016). To better understand migraine pathophysiology, diverse modalities of MRI have been employed in literature, being especially relevant those based on DMRI (Li et al., 2011; Yu et al., 2013; Chong and Schwedt, 2015). One particular study, carried out with the same database we will use in this work (Planchuelo-Gómez et al., 2020a), found significantly lower axial diffusivity (AD=λ_1) and MD values in chronic migraine (CM) compared to EM using tract-based spatial statistics (TBSS) (Smith et al., 2006), but no statistically significant differences were found between EM and HCs. In a recent study (Planchuelo-Gómez et al., 2020b) significant differences between patients with EM and HC were found using the RTOP calculated with AMURA over a single shell of $b = 1000$ s/mm^2. Patients with EM showed lower RTOP values than HC in 24 out of 48 the assessed regions from the ICBM-DTI-81 White Matter Atlas (Mori et al., 2008).

Hence, to test the moments with a different order, we will carry out a region-oriented analysis of the database in order to search for differences between EM and HC. For all the volumes, the FA was calculated using MRtrix (Tournier et al., 2019) from the data collected at $b = 1000$ s/mm^2. The FA maps of all the volumes were warped to a common template using the standard TBSS pipeline (Smith et al., 2006). The same transformation was applied to all the metrics considered for the experiment. A ROIs-based analysis was carried out: 48 different ROIs were identified on the subjects using the JHU WM atlas (Mori et al., 2005). The average value of the metrics on the FA-skeleton inside each ROI was calculated within the 2% and 98% percentiles. Note that the measures are only calculated over the skeleton to obtain a more robust mea-

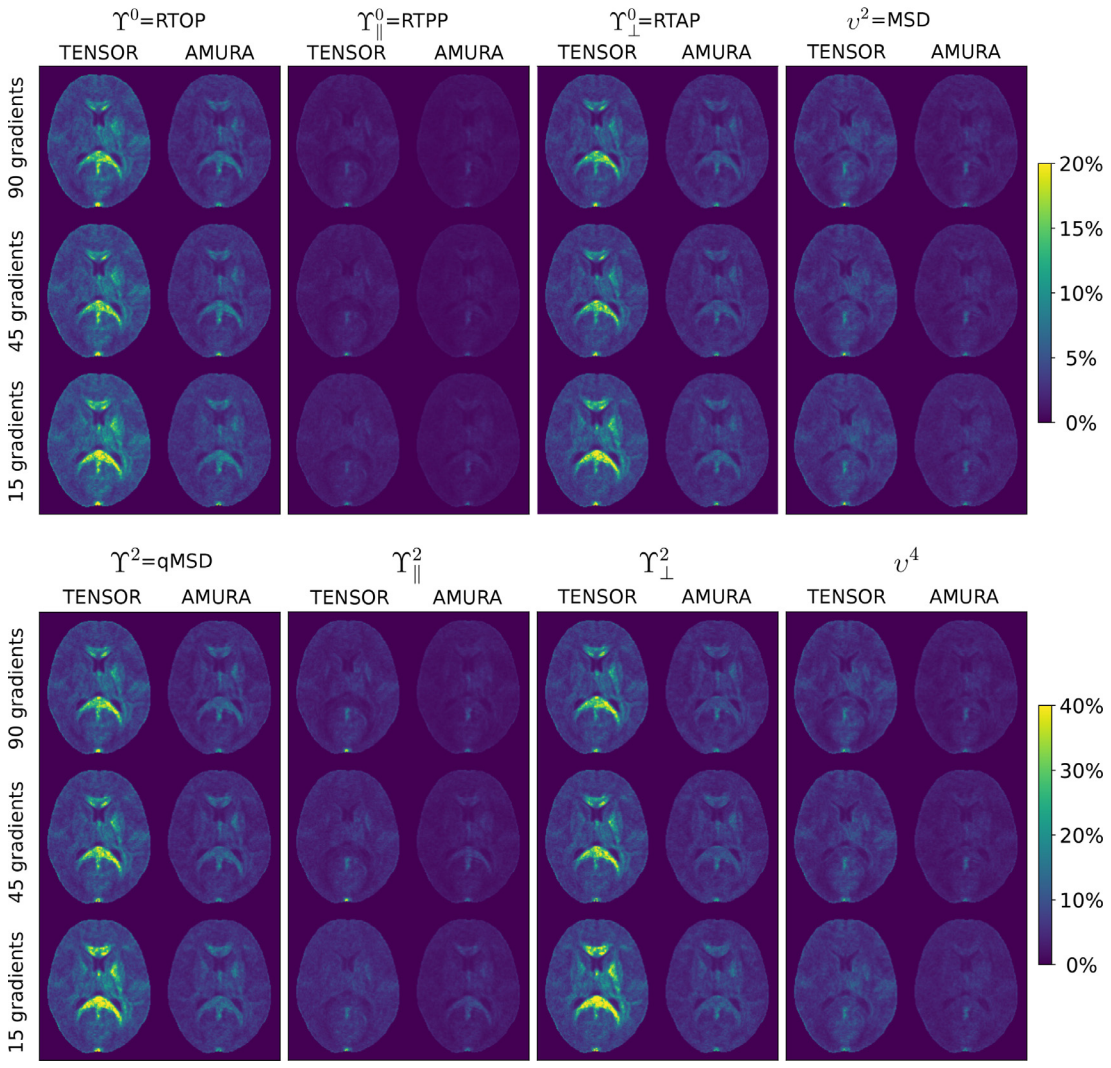

Fig. 8. Comparison of median CV maps, CV($\mathbf{x}$), obtained from the HCP WU-Minn test-retest database under different number of diffusion gradient directions employed to calculate the moments of $E(\mathbf{q})$ and $P(\mathbf{R})$, i.e. 90 (fully-sampled data), 45 and 15. The DT-based moments were obtained from a single-shell at $b = 1000$ s/mm^2, while the AMURA framework was applied to the data at $b = 3000$ s/mm^2.

sure. Then we carried out a two-sample-two-tailed, pooled variance t-test between HC and EM patients for each of the measures considered at each of the 48 ROIs. We corrected these results for multiple comparisons for each diffusion descriptor following the Benjamini-Hochberg False Discovery Rate (FDR) procedure. Note that our purpose is not to carry out a complete clinical study but to analyze the behavior of each measure separately. Thus, results may vary with those reported in literature, especially considering that the statistical comparisons are distinct in the present study, and they should not be roughly interpreted to determine clinical differences (which have already been validated elsewhere Planchuelo-Gómez et al., 2020a; Planchuelo-Gómez et al., 2020b).

Fourteen different measures were considered for the analysis: three DT-based measures (FA, AD, MD) and 11 AMURA-based (APA, Y^0 (RTOP), Y^2 (qMSD), $Y^{1/2}$, $Y^0_{||}$ (RTPP), $Y^1_{||}$, $Y^0_{\perp}$ (RTAP), $Y^2_{\perp}$, υ^1, υ^2 (MSD) and υ^{-1}). Figure 10 shows a p-value scheme for the 48 ROIs considered for each of the measures. Those ROIs that exhibit differences with statistical significance (before multiple comparison correction and FDR) above 95% ($p < 0.05$) are highlighted in green, above 99% ($p < 0.01$) in amber, and above 99.9% ($p < 0.001$) in yellow. Those ROIs that exhibit differences with statistical significance after multiple comparison correction and FDR are marked by a star (*). In the bottom of the figure the number of regions of each kind for every measure are also shown.

Basic metrics based on the DT show a limited amount of differences, with only one ROI with statistically significant differences for the MD and none for the FA and AD after the FDR correction. This result is consistent with the literature in which, after proper statistical corrections, none are found. For the sake of comparison, another anisotropy metric has been added, PA calculated with AMURA, which can be seen as an alternative to the FA. In this particular experiment PA proves to be more sensitive to changes than FA, coherently with results reported in (Aja-Fernández et al., 2021).

On the other hand, AMURA-based RTOP shows differences in nine regions after the correction for multiple comparisons. Once more, this is totally compatible with what we have seen in previous studies (Planchuelo-Gómez et al., 2020a): AMURA can detect changes between EM and HC where DTI cannot. In addition, qMSD (Y^2) shows a behavior similar to RTOP but, in this particular case, it provides a higher number of statistically significant differences (23 ROIs vs. 9, respectively, after the FDR correction), which is related to the higher number of statistically significant results for lower p-values set as threshold for statistical significance (see *Full* $E(\mathbf{q})$,

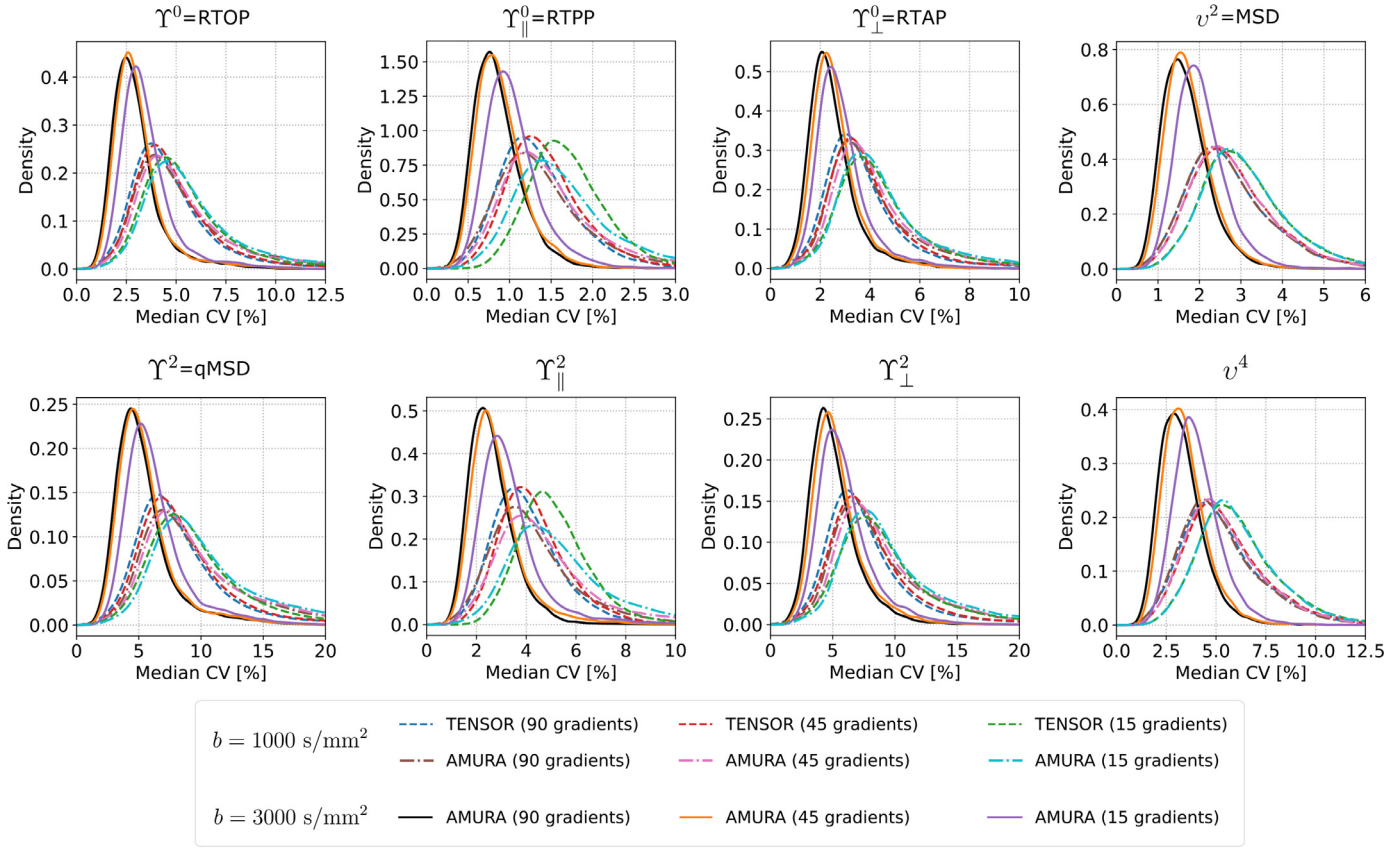

Fig. 9. The histograms of median CV maps for DT- and AMURA-based moments obtained from randomly three subjects from the HCP WU-Minn test-retest database under different numbers of diffusion gradient directions employed to calculate the moments of $E(\mathbf{q})$ and $P(\mathbf{R})$, i.e. 90 (fully-sampled data), 45 and 15. The DT-based moments were obtained from a single-shell at $b = 1000$ s/mm^2, while the AMURA framework was applied to the data at $b = 1000$ s/mm^2 and $b = 3000$ s/mm^2. Each curve presents a kernel density estimated plot for the histogram of the CV map of the measure under a specified method and the number of gradient directions used to calculate the parameter.

first two columns of Fig. 10). All the ROIs in qMSD show consistently smaller p-values than those in RTOP. Otherwise, the use of a non even moment like $Y^{1/2}$ does not seem particularly advantageous within this study.

RTAP and RTPP show a limited number of regions with differences after the FDR correction, in line with the findings in the literature. These two metrics would require a higher b-value in order to be more discriminant. However, in the planar case, note that when the order of the moments increases the number of statistically significant differences also increases, considering the unadjusted and the corrected results. For teh axial case, this effect is only visible in the unadjusted case.

Finally, the moments of the $P(\mathbf{R})$ exhibit a behavior very similar to the DT indices, with only one region with statistically significant differences after the FDR correction, considering simultaneously the three measures. Actually, υ^2 can be seen as a version of the MD with different weighting.

6. Discussion and conclusions

AMURA was originally proposed as a method to infer microstructural information from single-shell acquisitions, with no need to specifically calculate the whole EAP. As stated in the original paper (Aja-Fernández et al., 2020), the metrics provided by this method must be seen as *apparent* versions of the original metrics for a specific shell. The method was initially intended to be used for high b-values (over 2000 s/mm^2), since that is the regime in which measures like RTOP, RTPP and RTAP are better described. However, recent studies, like the one in Planchuelo-Gómez et al. (2020b), have shown its good performance even for DTI-like acquisitions with b-values around 1000 s/mm^2. In its original formulation, AMURA provided only a small amount of metrics: RTOP, RTPP, RTAP and APA. In this work, we have generalized them in order to provide a greater set of measures based on the moments of $E(\mathbf{q})$ and $P(\mathbf{R})$. The original AMURA metrics can be seen as particular cases of the new proposal calculating new generic moments.

In this sense, AMURA aims at generically describing the diffusion signal through the computation of arbitrary order moments, analogously to the proposal in Zucchelli et al. (2020). There, the authors propose a framework to generate rotationally-invariant features from the SH coefficients fitted to the diffusion signal. These features are directly linked with the MD, FA, or the volume of the spherical signal, and can be directly derived from single-shell acquisitions as well. AMURA is not directly defined over the SH coefficients, but this mathematical formalism is only used for the purpose of efficient numerical calculus. Moreover, AMURA attains an alternative description beyond rotation invariants through the computation of planar and axial (i.e. directional) moments.

These generalizations are not just a simple mathematical effort to provide a theoretical framework to AMURA. On the contrary, the new measures allow to better quantify different aspects of the diffusion in the brain, dealing with different features of the diffusion process and being particularly sensitive to the restricted components of such diffusion and better suited to deal with multiple meso-structure diffusion components than DT-based metrics. As we have shown in Fig. 10, different ponderations of the same signal will yield to different results and, in the case of clinical

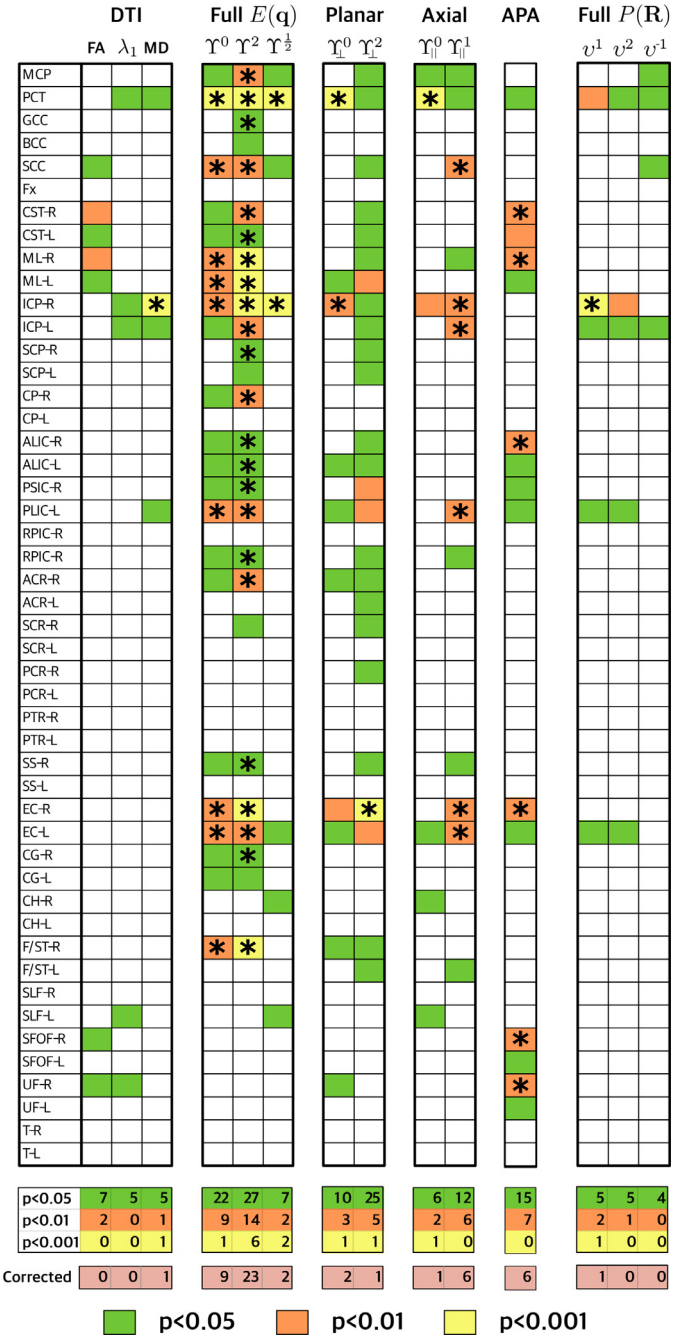

Fig. 10. Episodic migraine (EM) vs. healthy controls (HC): two-sample t-tests for different measures calculated for EMDb database at $b = 1000$ s/mm^2 and at each of 48 ROIs defined by the ICBM-DTI-81 atlas (the lower the better). The p-values represent the probability that the measure has identical means for both controls and patients. Differences with statistical significance above 95% are highlighted in green, above 99% in amber and above 99.9% in yellow. At the bottom, the number of regions showing significant differences between EM and HC for each measure. We have carried out the correction for multiple comparisons for each measure following the Benjamini-Hochberg false discovery rate (FDR) procedure. Regions with statistically significant differences between both groups after correction are marked with a star (*). (For interpretation of the references to colour in this figure legend, the reader is referred to the web version of this article.)

studies, could yield to discover new variability patterns in some pathologies, as we have illustrated in the case of migraine.

Although AMURA only needs one shell in order to calculate the different measures, the information provided is not the same obtained from the DT. Differences can be clearly seen in Fig. 3 and the test-retest experiment. The use of the DT assumes not only a Gaussian decay, but also a single-bundle meso-structure, while AMURA uses a generic $D(\mathbf{u})$ that could take into account arbitrary fiber bundles orientations. In the experiment carried out, we could see that the DT approach underestimates the values of the moments in those regions in which there is a complex fiber structure, like the centrum semiovale and the corpus callosum. In the former, different alignments and crossing-fiber structures cannot be properly described by the DT, while in the latter, the source of error is the high sub-voxel curvature of the fibers. Nevertheless, according to this particular experiment, moments calculated over the $E(\mathbf{q})$ are better estimated using a non-parametric orientation distribution, especially those moments of higher order. Results in this experiment are coherent with those obtained using more complex schemes, like MiSFIT (see Figs. 4 and 5 in Tristán-Vega and Aja-Fernández, 2021).

These results are also confirmed when we compared the *apparent* moments provided by AMURA with the *actual* moments estimated by a multishell approach, specifically MiSFIT. Although there are some clear differences in Fig. 4, for higher b-values, full and planar moments of the $E(\mathbf{q})$ show high correlation between both techniques. AMURA scalars present a reduced contrast when compared to MiSFIT, especially for the highest values of each moment. On the other hand, axial moments are the least robust ones, since they are computed over the $\mathbf{q}$-space samples along the maximum diffusion direction, for which the attenuation is maximal and the SNR dramatically decreases. We can conclude that AMURA does not produce totally analogous values to EAP-based approaches, one issue already raised in Aja-Fernández et al. (2020). However, the large correlations between both methods suggest that these measures are not considering totally different diffusion features, but very close ones. Once again, the goal of AMURA is not estimating the exact same values as EAP-based methods. Nevertheless, a shifted version of a given moment as the ones provided, could also be equally valuable when studying diffusion.

The reproducibility study showed, in general, a good agreement between test and retest acquisitions verified over 37 subjects. The AMURA measures retrieved at $b = 1000$ s/mm^2 presented a similar behavior to the DT but with a smaller variation in those areas with higher FA, coherently with the previous experiment. In addition, once the b-value increases, starting from $b = 2000$ s/mm^2, our results suggest that AMURA outperforms the DT equivalents in terms of CV. These results seem promising once applying the non-zeroth-order moments of $E(\mathbf{q})$ and $P(\mathbf{R})$ to clinical studies under the higher b-value regime, like those studies where the primary zeroth-order EAP-based moments have already been implemented and showed an advantage over the standard protocols (Brusini et al., 2016; Boscolo Galazzo et al., 2018; Ma et al., 2020; Le et al., 2020; Moody et al., 2021). One can observe amplified CV values for highly anisotropic brain regions, principally for the DT based measures, i.e. corpus callosum, fornix and limb of the internal capsule (see Fig. 7). The exaggerated values are remarkably noticeable with the full Y^p and planar $Y^p_\perp$ moments, especially the second-order ones. This effect can be explained on the ground of the tensor equations in Appendix B, as in the case of prolate tensors, we observe a positive/negative bias on the second/third eigenvalue, while in oblate tensors, representing crossing fibers, the second and third eigenvalues are generally underestimated (Whitcher et al., 2008). Therefore, special care must be taken once using higher-order moments, especially under the low b-value regime, as it might introduce a potential bias in the cohort studies. Nevertheless, the AMURA framework exhibits the robustness to a greatly limited number of the samples in the $\mathbf{q}$–space domain (e.g. only 15 samples per shell), allowing to significantly shorten the acquisition time while preserving the same amount of information. Notice that using only 15 gradient directions, the DT-based moments show intensified CV once compared to fully-

sampled data with 90 directions (see Fig. 8). Although no studies were performed on the influence of confounding factors on DT-based moments, one can presume that at least 30 gradient directions are suggested for robust estimation, like in the case of FA parameter (Jones, 2004).

The robustness of AMURA-based moments has been quantitatively confirmed using the histogram-based study presented in Fig. 9. The peak values of kernel density estimated curves are only slightly shifted towards increased median CV value once reducing the number of gradients to only 15 directions. Overall, the reproducibility and robustness to a reduced acquisition scenario experiments allowed recognizing the potential application of the AMURA approach in studies concerning the variability of the brain anatomy, such as longitudinal or lifespan studies, in which a high level of reproducibility is a must.

Finally, in the migraine experiment, AMURA shows a better performance than DT metrics, although we must clarify that this could not be the case for every other study. We have selected one for which, according to the literature, AMURA succeeds in finding differences where the DT could not. But in the same study (Planchuelo-Gómez et al., 2020b), AMURA could find almost no differences between EM and CM, while the DT succeeds. This effect talks about complementary measures, rather than competitive. On the other hand, this experiment allows us to better understand the behavior of different orders and kinds of moments of AMURA. According to the results in Fig. 10, the use of higher order moments in $\mathbf{q}$–space provides smaller p-values and allows finding a higher number of statistically significant differences between groups. This could be motivated by the fact that differences between EM and HC are subtle and these moments precisely highlight them. In general, the use of different moments could provide meaningful insight to different phenomenons of diffusion in the tissues, though further validation of AMURA moments is required to postulate them as clinical biomarker candidates.

Furthermore, metrics derived with AMURA have also shown larger correlation with multishell moments when higher b-values where considered. The acquisition of one single shell at b-values over 2000 s/mm^2 is not totally compatible with DT estimation, but it is consistent with single-shell HARDI techniques, in which the ODF is estimated and then some metrics could be derived, such as the ADC, the MD, the generalized FA (GFA) or the apparent fiber density (AFD) (Descoteaux, 1999). Once more, scalars derived from the ODF and moments from AMURA can be calculated together without extra-cost and be used complementarily in practical studies. The complementary nature of GFA and APA, for instance, was already shown in Aja-Fernández et al. (2021).

With regard to those moments based on the $P(\mathbf{R})$, they showed themselves not particularly interesting for clinical studies to the extent of the present paper: Fig. 3 shows a very high correlation between these indices calculated with either AMURA or the DT, putting at stake the added value of AMURA over DT in this case. When compared with a multishell approach like MiSFIT, these moments calculated with AMURA present a very low correlation with the actual values. In addition, the results of the migraine experiment also show a discriminant power similar to the DT-based measures and no added value. Thus, we must conclude that AMURA is not able to properly estimate the moments of $P(\mathbf{R})$. Unlike moments based on $E(\mathbf{q})$, for which a unique value of $\|\mathbf{q}\|$ allows to extrapolate an apparent behavior for the entire $\mathbf{q}$-space through modeling, a unique $\|\mathbf{q}\|$ sample does not allow a proper description of the bandwidth of the dual domain $\mathbf{R}$: results obtained with just one shell, although feasible from a theoretical point of view, do not provide significant information.

The computation of moments as proposed in this paper is based on the same implementation as in the original AMURA paper (Aja-Fernández et al., 2020), hence it shares similar pros and cons: since the reconstruction of the EAP is not explicitly required, the computation of scalar measurements will not impose a computational burden to the standard protocols; an entire volume can be processed in minutes or even seconds, so that a whole database for a clinical study can be processed in the order of few hours. On the other hand, one major drawback of these measures is the same pointed out in Aja-Fernández et al. (2020): the explicit assumption of a specific radial behavior for the diffusion, which cannot fit the whole $\mathbf{q}$–space. As a consequence, the selection of a single shell will make the anatomical features dependent on the selected b-value and, consequently, they must be considered *apparent*. This effect was confirmed by experiment in Fig. 6 and it implies that, in clinical studies, the results can be compared against each other only if the same b-value is preserved across data sets. However, despite the dependence with the b-value, the *apparent* moments calculated with AMURA have also shown a great correlation with the *actual* moments calculated with a multishell approach, especially for higher b-values.

All in all, the newly introduced AMURA moments can be easily integrated into the processing pipeline of currently existing single-shell DMRI protocols and databases to unveil anatomical details that may remain hidden in traditional DT-based studies. Their simplicity and fast calculation make them proper complementary metrics for clinical studies.

Software

The full implementation of the methods here included are part of the dMRI-Lab toolbox and it may be downloaded for MATLAB© (The MathWorks, Inc., Natick, MA) and GNU Octave, together with use-case examples and test data, from: http://www.lpi.tel.uva.es/dmrilab.

Declaration of Competing Interest

The authors declare no conflict of interest. The funders had no role in the design of the study; in the collection, analyses or interpretation of data; in the writing of the manuscript or in the decision to publish the results.

CRediT authorship contribution statement

Santiago Aja-Fernández: Conceptualization, Methodology, Software, Validation, Formal analysis, Investigation, Writing – original draft, Writing – review & editing, Supervision, Project administration, Funding acquisition. **Tomasz Pieciak:** Validation, Formal analysis, Investigation, Writing – original draft, Writing – review & editing. **Carmen Martín-Martín:** Validation, Formal analysis, Investigation, Data curation, Writing – original draft, Writing – review & editing. **Álvaro Planchuelo-Gómez:** Methodology, Validation, Formal analysis, Investigation, Data curation, Writing – original draft, Writing – review & editing. **Rodrigo de Luis-García:** Methodology, Validation, Formal analysis, Investigation, Writing – original draft. **Antonio Tristán-Vega:** Conceptualization, Methodology, Software, Validation, Formal analysis, Investigation, Writing – original draft, Writing – review & editing, Supervision.

Acknowledgments

This work was supported by Ministerio de Ciencia e Innovación of Spain with research grant RTI2018-094569-B-I00. Tomasz Pieciak acknowledges the Polish National Agency for Academic Exchange for grant PN/BEK/2019/1/00421 under the Bekker programme and the Ministry of Science and Higher Education (Poland) under the scholarship for outstanding young scientists (692/STYP/13/2018). Álvaro Planchuelo-Gómez was supported by

Junta de Castilla y León (Spain) and the European Social Fund (ID: 376062, Base de Datos Nacional de Subvenciones).

Extra data for this project was provided by (1) the *Human Connectome Project* (HCP; Principal Investigators: Bruce Rosen, M.D., Ph.D., Arthur W. Toga, Ph.D., Van J. Weeden, MD). HCP funding was provided by the National Institute of Dental and Craniofacial Research (NIDCR), the National Institute of Mental Health (NIMH), and the National Institute of Neurological Disorders and Stroke (NINDS). HCP data are disseminated by the Laboratory of Neuro Imaging at the University of Southern California; (2) Cardiff University Brain Research Imaging Centre, provided by Chantal Tax. The data were acquired at the UK National Facility for In Vivo MR Imaging of Human Tissue Microstructure funded by the EPSRC (grant EP/ M029778/1), and The Wolfson Foundation.

Appendix A. Calculation of full moments of $P(\mathbf{R})$

A1. Fourier transform in spherical coordinates

Let $D(\mathbf{u}) > 0$ be the diffusivity for a given *shell* $q = q_0$. Using the mono-exponential model, the diffusion signal can be defined as:

$$E(\mathbf{q}) = E(q\mathbf{u}) = \exp\left(-\frac{q^2}{q_0^2}D(\mathbf{u})\right), \tag{A.1}$$

where $\mathbf{u} \in \mathcal{S}$ is a unit direction in space. Since both $E(\mathbf{q})$ and $P(\mathbf{R})$ are real signals, the Eq. (1) may as well be established in terms of cosine functions instead of complex exponentials. Besides, it is convenient to represent the integrals in spherical coordinates:

$$\begin{aligned} P(\mathbf{R}) = P(R\mathbf{r}) &= \int_{\mathcal{S}} \left(\int_0^\infty q^2 E(q\mathbf{u}) \cos\left(2\pi q R \mathbf{u}^T\mathbf{r}\right) dq \right) d\mathbf{u} \\ &= \int_{\mathcal{S}} \left(\int_0^\infty q^2 \exp\left(-\frac{q^2}{q_0^2}D(\mathbf{u})\right) \cos\left(2\pi q R \mathbf{u}^T\mathbf{r}\right) dq \right) d\mathbf{u}, \end{aligned} \tag{A.2}$$

where $\mathbf{r} \in \mathcal{S}$ is a unit direction independent on $\mathbf{u}$. The inner integral in the variable q can be explicitly solved to yield (see Section 3.952, Eq. (4) in Gradshteyn and Ryzhik, 2014):

$$\begin{aligned} P(R\mathbf{r}) = \frac{\sqrt{\pi} q_0^3}{4} \int_{\mathcal{S}} D^{-\frac{3}{2}}(\mathbf{u}) \left(1 - \frac{2\left(\pi q_0 R \mathbf{u}^T\mathbf{r}\right)^2}{D(\mathbf{u})}\right) \\ \exp\left(-\frac{\left(\pi q_0 R \mathbf{u}^T\mathbf{r}\right)^2}{D(\mathbf{u})}\right) d\mathbf{u}. \end{aligned} \tag{A.3}$$

A2. Explicit computation of full moments

The pth full moment of the diffusion propagator is defined as:

$$\upsilon^p \triangleq \int_{\mathbb{R}^3} R^p P(\mathbf{R}) d\mathbf{R} = \int_{\mathcal{S}} \left(\int_0^\infty R^{p+2} P(R\mathbf{r}) dR \right) d\mathbf{r}, \tag{A.4}$$

where the integral is already represented in spherical coordinates. By casting Eq. (A.3) into the previous expression, the order of the integrals can be exchanged at convenience to obtain:

$$\begin{aligned} \upsilon^p = \frac{\sqrt{\pi} q_0^3}{4} \int_{\mathcal{S}} D^{-\frac{3}{2}}(\mathbf{u}) \int_0^\infty R^{p+2} \int_{\mathcal{S}} \left(1 - \frac{2\left(\pi q_0 R \mathbf{u}^T\mathbf{r}\right)^2}{D(\mathbf{u})}\right) \\ \exp\left(-\frac{\left(\pi q_0 R \mathbf{u}^T\mathbf{r}\right)^2}{D(\mathbf{u})}\right) d\mathbf{r}\, dR\, d\mathbf{u}. \end{aligned} \tag{A.5}$$

The innermost integral in the variable $\mathbf{r}$ can then be computed using regular spherical coordinates by just aligning their 'z' axis (i.e. the origin of the polar angle $\theta = 0$) with each $\mathbf{u}$, so that $\mathbf{u}^T\mathbf{r} = \cos\theta$:

$$\begin{aligned} &\int_{\mathcal{S}} \left(1 - \frac{2\left(\pi q_0 R \mathbf{u}^T\mathbf{r}\right)^2}{D(\mathbf{u})}\right) \exp\left(-\frac{\left(\pi q_0 R \mathbf{u}^T\mathbf{r}\right)^2}{D(\mathbf{u})}\right) d\mathbf{r} \\ &= \int_0^{2\pi} \int_0^{\pi} \left(1 - \frac{2(\pi q_0 R \cos\theta)^2}{D(\mathbf{u})}\right) \exp\left(-\frac{(\pi q_0 R \cos\theta)^2}{D(\mathbf{u})}\right) \sin\theta\, d\phi\, d\theta \\ &= 2\pi \int_{-1}^{1} \left(1 - \frac{2(\pi q_0 R s)^2}{D(\mathbf{u})}\right) \exp\left(-\frac{(\pi q_0 R s)^2}{D(\mathbf{u})}\right) ds \\ &= 4\pi \exp\left(-\frac{(\pi q_0 R)^2}{D(\mathbf{u})}\right), \end{aligned} \tag{A.6}$$

where the last integral is solved with the change of variable $s = \cos(\theta)$. This result is casted into Eq. (A.5) to obtain:

$$\begin{aligned} \upsilon^p &= \pi^{\frac{3}{2}} q_0^3 \int_{\mathcal{S}} D^{-\frac{3}{2}}(\mathbf{u}) \int_0^\infty R^{p+2} \exp\left(-\frac{(\pi q_0 R)^2}{D(\mathbf{u})}\right) dR \\ d\mathbf{u} &= \frac{\Gamma\left(\frac{p+3}{2}\right)}{2 q_0^p \pi^{p+\frac{3}{2}}} \int_{\mathcal{S}} D^{\frac{p}{2}}(\mathbf{u}) d\mathbf{u}, \end{aligned} \tag{A.7}$$

whose convergence is assured if $p > -3$. The latter integral has to be numerically computed for each acquired signal, which can be trivially attained by expanding $D^{\frac{p}{2}}$ over $\mathcal{S}$ using SHs. This way, the integral becomes a scaled version of the DC component, $C_{0,0}$, of such expansion:

$$\begin{aligned} \upsilon^p &= \frac{\Gamma\left(\frac{p+3}{2}\right)}{2 q_0^p \pi^{p+\frac{3}{2}}} \int_{\mathcal{S}} D^{\frac{p}{2}}(\mathbf{u}) d\mathbf{u} = \frac{\Gamma\left(\frac{p+3}{2}\right)}{2 q_0^p \pi^{p+\frac{3}{2}}} 2\sqrt{\pi} C_{0,0} \left\{ D^{\frac{p}{2}}(\mathbf{u}) \right\} \\ &= \frac{\Gamma\left(\frac{p+3}{2}\right)}{q_0^p \pi^{p+1}} C_{0,0} \left\{ D^{\frac{p}{2}}(\mathbf{u}) \right\}. \end{aligned} \tag{A.8}$$

Appendix B. Calculation of the moments using the diffusion tensor

If a Gaussian diffusion propagator is assumed, $P(\mathbf{R})$ is a mixture of independent and (nearly) identically distributed bounded cylinder statistics and, by virtue of the central limit theorem, their superposition is Gaussian distributed. The measured signal in the $\mathbf{q}$–space is the (inverse) Fourier transform of the PDF and it can be expressed as:

$$E(\mathbf{q}) = \mathcal{F}^{-1}\{P(\mathbf{R})\}(\mathbf{q}) = \exp\left(-4\pi^2 \tau \mathbf{q}^T \mathcal{D} \mathbf{q}\right), \tag{B.1}$$

which represents the well-known Stejskal–Tanner equation (Stejskal and Tanner, 1965). The diffusion tensor $\mathcal{D}$ is the anisotropic covariance matrix of the Gaussian PDF $P(\mathbf{R})$, and therefore it is a symmetric, positive–definite matrix with real, positive eigenvalues ($\lambda_1 \geq \lambda_2 \geq \lambda_3$) and orthonormal eigenvectors.

We can use this model to estimate the generalized moments of $E(\mathbf{q})$ and $P(\mathbf{R})$ defined in Sections 3.1 and 3.2. For the sake of simplicity, only the even moments are calculated (the only ones with closed-form expressions):

1. Full moments of $E(\mathbf{q})$:

$$\begin{aligned} Y^p = \frac{1}{(4\pi^2\tau)^{\frac{3+p}{2}}} \sum_{k=0}^{p/2} \sum_{m=0}^{k} \binom{p/2}{k} \binom{k}{m} \\ \times \frac{\Gamma\left(\frac{1}{2}+k-m\right)\Gamma\left(\frac{1}{2}+m\right)\Gamma\left(\frac{1}{2}+\frac{p}{2}-k\right)}{\lambda_1^{\frac{p}{2}+\frac{1}{2}-k}\, \lambda_2^{k-m+\frac{1}{2}}\, \lambda_3^{m+\frac{1}{2}}}. \end{aligned} \tag{B.2}$$

This solution is valid for $p \geq 0$ and only for p integer and even. Some specific values are:

$$Y^0 = \frac{\pi^{3/2}}{(4\pi^2\tau)^{3/2}} \frac{1}{\sqrt{\lambda_1\lambda_2\lambda_3}} \qquad \text{(RTOP)};$$

$$Y^2 = \frac{\pi^{3/2}}{2(4\pi^2\tau)^{5/2}} \frac{\lambda_1\lambda_2 + \lambda_2\lambda_3 + \lambda_1\lambda_3}{(\lambda_1\lambda_2\lambda_3)^{3/2}} \quad \text{(qMSD)}.$$

2. Axial moments of $E(\mathbf{q})$:

$$Y^p_{||} = \frac{\Gamma\left(\frac{1+p}{2}\right)}{(4\pi^2\tau)^{\frac{1+p}{2}} \lambda_1^{\frac{1+p}{2}}}. \tag{B.3}$$

This solution is valid for $p > -1$. For example:

$$Y^0_{||} = \frac{\sqrt{\pi}}{\sqrt{4\pi^2\tau}} \frac{1}{\sqrt{\lambda_1}} \quad \text{(RTPP)};$$

$$Y^2_{||} = \frac{\sqrt{\pi}}{2(4\pi^2\tau)^{3/2}} \frac{1}{\lambda_1^{3/2}}.$$

3. Planar moments of $E(\mathbf{q})$:

$$Y^p_{\perp} = \frac{1}{(4\pi^2\tau)^{\frac{p}{2}+1}} \sum_{k=0}^{p/2} \binom{p/2}{k} \frac{\Gamma\left(\frac{1}{2}+k\right)\Gamma\left(\frac{1}{2}+\frac{p}{2}-k\right)}{\lambda_2^{-k+\frac{p}{2}+\frac{1}{2}} \lambda_3^{k+\frac{1}{2}}}. \tag{B.4}$$

This solution is valid for $p \geq 0$ and only for p integer and even. Some specific values are

$$Y^0_{\perp} = \frac{\pi}{4\pi^2\tau} \frac{1}{\sqrt{\lambda_2\lambda_3}} \quad \text{(RTAP)};$$

$$Y^2_{\perp} = \frac{\pi}{2(4\pi^2\tau)^2} \frac{\lambda_2+\lambda_3}{(\lambda_2\lambda_3)^{3/2}}.$$

4. Full moments of $P(\mathbf{R})$:

$$\upsilon^p = \frac{1}{q_0^p \pi^{3+p}} \sum_{k=0}^{p/2} \sum_{m=0}^{k} \phi^{\upsilon}_{pkm} \lambda_1^{\frac{p}{2}-k} \lambda_2^{k-m} \lambda_3^{m}; \tag{B.5}$$

$$\phi^{\upsilon}_{pkm} = \binom{p/2}{k} \binom{k}{m} \Gamma\left(\frac{1}{2}+k-m\right)\Gamma\left(\frac{1}{2}+m\right)\Gamma\left(\frac{1}{2}+\frac{p}{2}-k\right).$$

This solution is valid for $p \geq 0$ and only for p integer and even. Some specific values are:

$$\upsilon^0 = 1;$$

$$\upsilon^2 = \frac{1}{2\pi^2 q_0^2}(\lambda_1+\lambda_2+\lambda_3) \quad \text{(MSD)};$$

$$\upsilon^4 = \frac{1}{4\pi^4 q_0^4}\left[2(\lambda_1^2+\lambda_2^2+\lambda_3^2) + (\lambda_1+\lambda_2+\lambda_3)^2\right].$$

References

Aboitiz, F., Lopez Calderon, J., Montiel, J., 2003. Long distance communication in the human brain: timing constraints for inter-hemispheric synchrony and the origin of brain lateralization. Biol. Res. 36, 89–99.

Aboitiz, F., Scheibel, A., Fisher, R., Zaidel, E., 1992. Fiber composition of the human corpus callosum. Brain Res. 598, 143–153.

Aja-Fernández, S., de Luis-García, R., Afzali, M., Molendowska, M., Pieciak, T., Tristán-Vega, A., 2020. Micro-structure diffusion scalar measures from reduced MRI acquisitions. PLoS ONE 15 (3), e0229526.

Aja-Fernández, S., Niethammer, M., Kubicki, M., Shenton, M.E., Westin, C.-F., 2008. Restoration of DWI data using a Rician LMMSE estimator. IEEE Trans. Med. Imaging. 27 (10), 1389–1403.

Aja-Fernández, S., Tristán-Vega, A., Jones, D.K., 2021. Apparent propagator anisotropy from single-shell diffusion MRI acquisitions. Magn. Reson. Med. 85 (5), 2869–2881.

Assaf, Y., Mayk, A., Cohen, Y., 2000. Displacement imaging of spinal cord using q-space diffusion-weighted MRI. Magn. Reson. Med. 44 (5), 713–722.

Assemlal, H.-E., Tschumperlé, D., Brun, L., Siddiqi, K., 2011. Recent advances in diffusion MRI modeling: angular and radial reconstruction. Med. Image Anal. 15 (4), 369–396.

Basser, P., Pierpaoli, C., 1996. Microstructural features measured using diffusion tensor imaging. J. Magn. Reson. 111 (3), 209–219.

Basser, P.J., 2002. Relationships between diffusion tensor and q-space MRI. Magn. Reson. Med. 47 (2), 392–397.

Basser, P.J., Mattiello, J., LeBihan, D., 1994. MR diffusion tensor spectroscopy and imaging. Biophys. J. 66 (1), 259–267.

Bester, M., Jensen, J., Babb, J., Tabesh, A., Miles, L., Herbert, J., Grossman, R., Inglese, M., 2015. Non-gaussian diffusion MRI of gray matter is associated with cognitive impairment in multiple sclerosis. Mult. Scler. J. 21 (7), 935–944.

Boscolo Galazzo, I., Brusini, L., Obertino, S., Zucchelli, M., Granziera, C., Menegaz, G., 2018. On the viability of diffusion MRI-based microstructural biomarkers in ischemic stroke. Front. Neurosci. 12, 92.

Brusini, L., Obertino, S., Galazzo, I.B., Zucchelli, M., Krueger, G., Granziera, C., Menegaz, G., 2016. Ensemble average propagator-based detection of microstructural alterations after stroke. Int. J. Comput. Assist. Radiol. Surg. 11 (9), 1585–1597.

Brusini, L., Obertino, S., Zucchelli, M., Galazzo, I.B., Krueger, G., Granziera, C., Menegaz, G., 2015. Assessment of mean apparent propagator-based indices as biomarkers of axonal remodeling after stroke. In: Medical Image Computing and Computer-Assisted Intervention – MICCAI 2015. Springer International Publishing, pp. 199–206.

Callaghan, P., Eccles, C., Xia, Y., 1988. NMR microscopy of dynamic displacements: k-space and q-space imaging. J. Phys. E Sci. Instrum. 21 (8), 820.

Canales-Rodríguez, E.J., Lin, C.-P., Iturria-Medina, Y., Yeh, C.-H., Cho, K.-H., Melie-García, L., 2010. Diffusion orientation transform revisited. Neuroimage 49 (2), 1326–1339.

Chong, C.D., Schwedt, T.J., 2015. Migraine affects white-matter tract integrity: a diffusion-tensor imaging study. Cephalalgia 35 (13), 1162–1171.

De Luca, A., Ianus, A., Leemans, A., Palombo, M., Shemesh, N., Zhang, H., Alexander, D.C., Nilsson, M., Froeling, M., Biessels, G.-J., et al., 2021. On the generalizability of diffusion MRI signal representations across acquisition parameters, sequences and tissue types: chronicles of the MEMENTO challenge. Neuroimage 240, 1–17.

Descoteaux, M., 1999. High angular resolution diffusion imaging (HARDI). Wiley Encycl. Electr. Electron.Eng. 1–25.

Descoteaux, M., Angelino, E., Fitzgibbons, S., Deriche, R., 2007. Regularized, fast, and robust analytical Q-ball imaging. Magn. Reson. Med. 58, 497–510.

Descoteaux, M., Deriche, R., Le Bihan, D., Mangin, J.-F., Poupon, C., 2011. Multiple q-shell diffusion propagator imaging. Med. Image Anal. 15 (4), 603–621.

Fan, Q., Witzel, T., Nummenmaa, A., Van Dijk, K.R., Van Horn, J.D., Drews, M.K., Somerville, L.H., Sheridan, M.A., Santillana, R.M., Snyder, J., et al., 2016. MGH–USC human connectome project datasets with ultra-high b-value diffusion MRI. Neuroimage 124, 1108–1114.

Farrell, J.A., Landman, B.A., Jones, C.K., Smith, S.A., Prince, J.L., van Zijl, P.C., Mori, S., 2007. Effects of signal-to-noise ratio on the accuracy and reproducibility of diffusion tensor imaging–derived fractional anisotropy, mean diffusivity, and principal eigenvector measurements at 1.5T. J. Magn. Reson. Imaging 26 (3), 756–767.

Gradshteyn, I.S., Ryzhik, I.M., 2014. Table of Integrals, Series, and Products. Academic press.

Haije, T.D., Özarslan, E., Feragen, A., 2020. Enforcing necessary non-negativity constraints for common diffusion MRI models using sum of squares programming. Neuroimage 209, 116405.

Hosseinbor, A.P., Chung, M.K., Wu, Y.-C., Alexander, A.L., 2013. Bessel fourier orientation reconstruction (BFOR): an analytical diffusion propagator reconstruction for hybrid diffusion imaging and computation of q-space indices. Neuroimage 64, 650–670.

Hosseinbor, A.P., Chung, M.K., Wu, Y.-C., Fleming, J.O., Field, A.S., Alexander, A.L., 2012. Extracting quantitative measures from EAP: A small clinical study using BFOR. In: Med Image Comput Comput Assist Interv. Springer, pp. 280–287.

Jenkinson, M., Bannister, P., Brady, M., Smith, S., 2002. Improved optimization for the robust and accurate linear registration and motion correction of brain images. Neuroimage 17 (2), 825–841.

Jenkinson, M., Smith, S., 2001. A global optimisation method for robust affine registration of brain images. Med. Image Anal. 5 (2), 143–156.

Jensen, J.H., Helpern, J.A., Ramani, A., Lu, H., Kaczynski, K., 2005. Diffusional kurtosis imaging: the quantification of non-Gaussian water diffusion by means of magnetic resonance imaging. Magn. Reson. Med. 53 (6), 1432–1440.

Jones, D.K., 2004. The effect of gradient sampling schemes on measures derived from diffusion tensor MRI: a Monte Carlo study. Magn. Reson. Med. 51 (4), 807–815.

Karmacharya, S., Gagoski, B., Ning, L., Vyas, R., Cheng, H., Soul, J., Newberger, J., Shenton, M., Rathi, Y., Grant, P., 2018. Advanced diffusion imaging for assessing normal white matter development in neonates and characterizing aberrant development in congenital heart disease. Neuroimage Clin. 19, 360–373.

Katsarava, Z., Buse, D.C., Manack, A.N., Lipton, R.B., 2012. Defining the differences between episodic migraine and chronic migraine. Curr. Pain Headache Rep. 16 (1), 86–92.

Knösche, T.R., Anwander, A., Liptrot, M., Dyrby, T.B., 2015. Validation of tractography: comparison with manganese tracing. Hum. Brain Mapp. 36 (10), 4116–4134.

Le, H., Zeng, W., Zhang, H., Li, J., Wu, X., Xie, M., Yan, X., Zhou, M., Zhang, H., Wang, M., et al., 2020. Mean apparent propagator MRI is better than conventional diffusion tensor imaging for the evaluation of Parkinsons disease: a prospective pilot study. Front. Aging Neurosci. 12.

Li, X.L., Fang, Y.N., Gao, Q.C., Lin, E.J., Hu, S.H., Ren, L., Ding, M.H., Luo, B.N., 2011. A diffusion tensor magnetic resonance imaging study of corpus callosum from adult patients with migraine complicated with depressive/anxious disorder. Headache 51 (2), 237–245.

Lu, H., Jensen, J.H., Ramani, A., Helpern, J.A., 2006. Three-dimensional characterization of non-gaussian water diffusion in humans using diffusion kurtosis imaging. NMR Biomed. 19 (2), 236–247.

Ma, K., Zhang, X., Zhang, H., Yan, X., Gao, A., Song, C., Wang, S., Lian, Y., Cheng, J., 2020. Mean apparent propagator-MRI: a new diffusion model which improves temporal lobe epilepsy lateralization. Eur. J. Radiol. 126, 108914.

Moeller, S., Pisharady Kumar, P., Andersson, J., Akcakaya, M., Harel, N., Ma, R., Wu, X., Yacoub, E., Lenglet, C., Ugurbil, K., 2021. Diffusion imaging in the post HCP era. J. Magn. Reson. Imaging 54 (1), 36–57.

Moody, J., Dean III, D., Kecskemeti, S., Johnson, S., Bendlin, B., Alexander, A., 2021. Assessing white matter microstructural changes associated with aging & dementia using mean apparent propagator (MAP) MRI. In: Proc. Intl. Soc. Mag. Reson. Med., p. 1922.
Mori, S., Oishi, K., Jiang, H., Jiang, L., Li, X., Akhter, K., Hua, K., Faria, A.V., Mahmood, A., Woods, R., et al., 2008. Stereotaxic white matter atlas based on diffusion tensor imaging in an ICBM template. Neuroimage 40 (2), 570–582.
Mori, S., Wakana, S., Van Zijl, P.C., Nagae-Poetscher, L., 2005. MRI Atlas of Human White Matter. Elsevier.
Ning, L., Westin, C.-F., Rathi, Y., 2015. Estimating diffusion propagator and its moments using directional radial basis functions. IEEE Trans. Med. Imag. 34 (10), 2058–2078.
Özarslan, E., Koay, C.G., Shepherd, T.M., Komlosh, M.E., Irfanoğlu, M.O., Pierpaoli, C., Basser, P.J., 2013. Mean apparent propagator (MAP) MRI: a novel diffusion imaging method for mapping tissue microstructure. Neuroimage 78, 16–32.
Özarslan, E., Sepherd, T.M., Vemuri, B.C., Blackband, S.J., Mareci, T.H., 2006. Resolution of complex tissue microarchitecture using the diffusion orientation transform (DOT). Neuroimage 31, 1086–1103.
Pasternak, O., Westin, C.-F., Dahlben, B., Bouix, S., Kubicki, M., 2015. The extent of diffusion MRI markers of neuroinflammation and white matter deterioration in chronic schizophrenia. Schizophr. Res. 161 (1), 113–118.
Planchuelo-Gomez, Á., Garcia-Azorin, D., Guerrero, A.L., Aja-Fernández, S., Rodriguez, M., de Luis-Garcia, R., 2020. Structural connectivity alterations in chronic and episodic migraine: a diffusion magnetic resonance imaging connectomics study. Cephalalgia 40 (4), 367–383.
Planchuelo-Gómez, Á., García-Azorín, D., Guerrero, Á.L., Aja-Fernández, S., Rodríguez, M., de Luis-García, R., 2020. White matter changes in chronic and episodic migraine: a diffusion tensor imaging study. J. Headache Pain 21 (1), 1–15.
Planchuelo-Gómez, Á., García-Azorín, D., Guerrero, Á.L., Luis-García, R.d., Rodríguez, M., Aja-Fernández, S., 2020. Alternative microstructural measures to complement diffusion tensor imaging in migraine studies with standard MRI acquisition. Brain Sci. 10 (10), 711.
Planchuelo-Gómez, Á., Luis-García, R., García-Azorín, D., Guerrero, Á.L., Tristan-Vega, A., Aja-Fernández, S., 2021. AMURA with single-shell acquisitions detects additional white matter properties compared to the diffusion tensor in patients with persistent headache after COVID-19. In: Iberian ISMRM 1st Conference, p. 84.
Rovaris, M., Filippi, M., 2007. Diffusion tensor MRI in multiple sclerosis. J. Neuroimaging 17 (s1), 27S–30S.
Smith, S., Jenkinson, M., Johansen-Berg, H., et al., 2006. Tract-based spatial statistics: voxelwise analysis of multi-subject diffusion data. Neuroimage 31, 1487–1505.
Smith, S.M., Jenkinson, M., Woolrich, M.W., Beckmann, C.F., Behrens, T.E., Johansen-Berg, H., Bannister, P.R., De Luca, M., Drobnjak, I., Flitney, D.E., et al., 2004. Advances in functional and structural MR image analysis and implementation as FSL. Neuroimage 23, S208–S219.
Stejskal, E.-O., Tanner, J.-E., 1965. Spin diffusion measurements: spin echoes in the presence of a time-dependent field gradient. J. Chem. Phys. 42, 288–292.
Tournier, J.-D., Mori, S., Leemans, A., 2011. Diffusion tensor imaging and beyond. Magn. Reson. Med. 65 (6), 1532.
Tournier, J.-D., Smith, R., Raffelt, D., Tabbara, R., Dhollander, T., Pietsch, M., Christiaens, D., Jeurissen, B., Yeh, C.-H., Connelly, A., 2019. MRtrix3: a fast, flexible and open software framework for medical image processing and visualisation. Neuroimage 202, 116137.
Tristán-Vega, A., Aja-Fernández, S., 2021. Efficient and accurate EAP imaging from multi-shell dMRI with micro-structure adaptive convolution kernels and dual Fourier integral transforms (MiSFIT). Neuroimage 227, 117616.
Tristán-Vega, A., Aja-Fernández, S., Westin, C.-F., 2012. Least squares for diffusion tensor estimation revisited: propagation of uncertainty with Rician and non-Rician signals. Neuroimage 59 (4), 4032–4043.
Tuch, D.S., 2004. Q–ball imaging. Magn. Reson. Med. 52, 1358–1372.
Tuch, D.S., Reese, T.G., Wiegell, M.R., Wedeen, V.J., 2003. Diffusion MRI of complex neural architecture. Neuron 40, 885–895.
Van Essen, D.C., Smith, S.M., Barch, D.M., Behrens, T.E., Yacoub, E., Ugurbil, K., Consortium, W.-M.H., et al., 2013. The WU-minn human connectome project: an overview. Neuroimage 80, 62–79.
Westin, C.-F., Maier, S.E., Mamata, H., Nabavi, A., Jolesz, F.A., Kikinis, R., 2002. Processing and visualization for diffusion tensor MRI. Med. Image Anal. 6 (2), 93–108.
Whitcher, B., Tuch, D.S., Wisco, J.J., Sorensen, A.G., Wang, L., 2008. Using the wild bootstrap to quantify uncertainty in diffusion tensor imaging. Hum. Brain Mapp. 29 (3), 346–362.
Wu, Y.-C., Field, A.S., Alexander, A.L., 2008. Computation of diffusion function measures in q-space using magnetic resonance hybrid diffusion imaging. IEEE Trans. Med. Imag. 27 (6), 858–865.
Yu, D., Yuan, K., Qin, W., Zhao, L., Dong, M., Liu, P., Yang, X., Liu, J., Sun, J., Zhou, G., et al., 2013. Axonal loss of white matter in migraine without aura: a tract-based spatial statistics study. Cephalalgia 33 (1), 34–42.
Zhang, Y., Kong, Q., Chen, J., Li, L., Wang, D., Zhou, J., 2016. International classification of headache disorders 3rd edition beta-based field testing of vestibular migraine in china: demographic, clinical characteristics, audiometric findings and diagnosis statues. Cephalalgia 36 (3), 240–248.
Zucchelli, M., Brusini, L., Méndez, C.A., Daducci, A., Granziera, C., Menegaz, G., 2016. What lies beneath? Diffusion EAP-based study of brain tissue microstructure. Med. Image Anal. 32, 145–156.
Zucchelli, M., Deslauriers-Gauthier, S., Deriche, R., 2020. A computational framework for generating rotation invariant features and its application in diffusion MRI. Med. Image Anal. 60, 101597.